Energy Conversion and Management 274 (2022) 116222

Contents lists available at ScienceDirect

Energy Conversion and Management

journal homepage: www.elsevier.com/locate/enconman

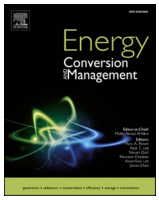

Thermo-economic analysis of steam accumulation and solid thermal energy storage in direct steam generation concentrated solar power plants

Abdullah A. Al Kindi [a], Paul Sapin [a], Antonio M. Pantaleo [a,b], Kai Wang [a,c], Christos N. Markides [a,*]

[a] Clean Energy Processes (CEP) Laboratory, Department of Chemical Engineering, Imperial College London, London SW7 2AZ, United Kingdom
[b] Department of Agro-environmental Sciences, University of Bari, Via Orabona 3, 70125 Bari, Italy
[c] Institute of Refrigeration and Cryogenics, Key Laboratory of Refrigeration and Cryogenic Technology of Zhejiang Province, Zhejiang University, Hangzhou 310027, China

ARTICLE INFO

Keywords:
Concentrated solar power
Power generation
Renewable energy
Solar energy
Steam accumulation
Steam turbines
Thermal energy storage

ABSTRACT

In direct steam generation (DSG) concentrated solar power (CSP) plants, a common thermal energy storage (TES) option relies on steam accumulation. This conventional option is constrained by temperature and pressure limits, and delivers saturated or slightly superheated steam at reduced pressure during discharge, which is undesirable for part-load turbine operation. However, steam accumulation can be integrated with sensible-heat storage in concrete to provide higher-temperature superheated steam at higher pressure. In this paper, this conventional steam accumulation option (existing) and an integrated concrete-steam TES option (extended) are described and analysed, and their thermo-economic performance are compared taking the 50-MW Khi Solar One DSG CSP plant in South Africa as a case study. The results show that the extended option with five 10-m long, square cross-section concrete blocks, each with 3600 equally spaced tubes, provides an additional TES capacity of 177 MWh compared to the existing configuration as a result of utilising most of the available thermal power in the solar receivers. Moreover, the extended option delivers 58 % more electricity with a 13 % enhancement in thermal efficiency during TES discharging mode. With an estimated additional investment of $4.2M, the levelised costs of storage and electricity for Khi Solar One with the extended TES option are, respectively, 29 % and 6 % lower than those obtained with the existing TES option. With the extended TES option, the projected net present value of Khi Solar One increases by 73 %, from $41M to $71M, at an average electricity price of 280 $/MWh.

1. Introduction

The decarbonisation of the energy sector is a pivotal element of the transition to a low-carbon and sustainable future and solar energy is already playing a leading role in this ongoing transition process. Solar power generation can be distributed [1], typically in smaller plants without or with simple optical complexity (i.e., concentration) and that are either intended primarily for electricity generation [2,3] or for heat and power cogeneration [4,5], or in larger, centralised plants. The latter solar power technologies are referred to as concentrated solar power (CSP) as they employ mirrors or lenses to concentrate a large area of the sunlight onto a receiver that transfers the concentrated power to a heat transfer fluid (HTF). The HTF is then directly or indirectly used to drive turbines for power generation as in most conventional power plants [6,7]. Direct steam generation (DSG) CSP is an option that uses water as a HTF in the solar receivers as well as a working fluid in the thermodynamic power generation cycle [8]. The use of a single fluid offers a number of benefits such as: (i) no need of heat exchangers for transferring heat between the HTF and the working fluid, which is the case in most conventional CSP plants [9–11]; (ii) enhanced cycle thermal efficiency by achieving higher steam temperatures [9–11]; (iii) removal of the environmental risk of fire and leakage [11]; and (iv) lower investment and operation & maintenance costs due to the elimination of heat exchangers [11].

Most solar power plants, irrespective of their scale (i.e., from smaller [12] to larger [13,14] plants), are coupled with thermal energy storage (TES) systems that store excess solar heat during daytime and discharge during night or during cloudy periods [15]. In DSG CSP plants, the typical TES options include: (i) direct steam accumulation; (ii) indirect sensible TES; and (iii) indirect latent TES [9]. Option (i) is considered as a direct method because the thermal energy is stored directly in the HTF. However, options (ii) and (iii) are indirect since thermal energy is stored in another storage medium such as solid-state storage medium, liquid-

* Corresponding author.
E-mail address: c.markides@imperial.ac.uk (C.N. Markides).

https://doi.org/10.1016/j.enconman.2022.116222
Received 22 June 2022; Received in revised form 6 September 2022; Accepted 7 September 2022

Nomenclature

Acronyms

CSP	concentrated solar power
DNI	direct normal irradiance
DSG	direct steam generation
HP	high pressure
HTF	heat transfer fluid
IRR	internal rate of return
LCOE	levelised cost of electricity
LCOS	levelised cost of storage
LP	low pressure
NPV	net present value
PCM	phase change material
PPA	power purchase agreement
RMSE	root mean square error
SA	steam accumulator
TES	thermal energy storage
WFR	water filling ratio

Symbols

A	area (m^2)
Bi	Biot number (–)
C	cost ($)
c	specific heat (J/kg K)
d	thickness (m)
D	diameter (m)
DE	discharged electricity (J, Wh)
DNI	direct normal irradiance (W/m^2)
e	absolute tube roughness (m)
f	friction factor (–)
F	cost factor (–)
g	acceleration of gravity (m/s^2)
G	mass flux (kg/m^2 s)
h	specific enthalpy (J/kg)
H	enthalpy (J) or height (m)
I	cost index (–) or revenues ($)
j	spatial node (–)
J	dimensionless velocity (–)
k	thermal conductivity (W/m K)
L	length (m)
$LCOE$	levelised cost of electricity ($/Wh)
$LCOS$	levelised cost of storage ($/Wh)
m	mass (kg)
$\dot{m}$	mass flowrate (kg/s)
n	time step (–) or lifetime (years)
N	number of units (–)
NPV	net present value ($)
$O\&M$	operation and maintenance costs ($)
P	pressure (Pa)
Pr	Prandtl number (–)
q	heat flux (W/m^2)
$\dot{Q}$	heat power (W)
r	discount rate (%)
R	radius (m)
Re	Reynolds number (–)
s	specific entropy (J/kg K)
t	time (s)
T	temperature (°C)
u	specific internal energy (J/kg)
U	unit price ($)
V	volume (m^3)
W	width (m) or weight (kg)
$\dot{W}$	power (W)
WFR	water filling ratio (–)
x	quality (–)
z	axial length (m)
Z	Shah's correlation parameter (–)

Greek symbols

α	heat transfer coefficient (W/m^2 K)
β	boundary constant (–)
γ	boundary constant (–)
Δ	change between two values (–)
$\in$	error (%)
η	efficiency (–)
μ	dynamic viscosity (kg/m s)
ν	specific volume (m^3/kg)
ρ	density (kg/m^3)
τ	total time (s)

Subscripts/superscripts

1 to 28	number of flow stream
$'$	saturated liquid
$''$	saturated vapour
a	ambient
A	analysis/present year
ava	availability
avg	average
B	base year
BM	bare module
C	concrete mixture
CB	concrete block
Ch	charging
CP	condensate pump
crit	critical
Cyc	power generation cycle
DE	deaerator
Dch	discharging
e	effective
E	electrical
evp	evaporator
exp	experimental
f	fluid
F	foundation
FP	feedwater pump
gen	generator
h	hydraulic
hel	heliostat
HFWH	high-pressure feedwater heater
HX	heat exchanger
i	inner
I&C	instruments and control
in	inlet
Ins	insulation
irr	irradiance
is	isentropic
L	liquid
LFWH	low-pressure feedwater heater
LM	logarithmic mean
Lo	all liquid
loss	loss
M	material
net	net
nom	nominal
Nu	Nusselt
o	outer
OB	on-board
out	outlet
P	purchase or pressure

P&S	platform and steel	Sh	Shah
P&V	piping and valves	SP	single phase
P1	Part 1	spr	superheater
P2	Part 2	ST	solar tower
P3	Part 3	T	turbine
P4	Part 4	TES	thermal energy storage
PL	platform and ladders	TP	two-phase or turbo-pump
pp	pinch point	tubes	tubes
R	reduced	total	total
s	solid or surface	V	vapour
SA	steam accumulator	vap	vaporisation
sat	saturation	w	wall

state storage medium, or phase-change materials (PCMs) [9].

Steam accumulation is the simplest TES technology for DSG as steam is directly stored in a storage pressure vessel, i.e., steam accumulator (SA), in form of pressurised saturated water [16]. Discharging from SAs usually takes place from the top part of the vessel as it is filled with saturated steam at the saturation pressure. Steam accumulation is commercially available and was implemented in several operating DSG power plants, such as the PS10 plant in Spain, and the Khi Solar One plant in South Africa [17]. A major disadvantage of steam accumulation is the relatively low temperature of the outlet saturated steam (i.e., a maximum temperature of 374 °C) when compared to the operating temperatures of DSG plants, which could reach up to 550 °C [18]. Reaching the maximum temperature of 374 °C is not a cost-effective option as reaching this temperature in saturated conditions also means reaching the water critical pressure (22.1 MPa), and designing a pressure vessel that could withstand this high pressure requires expensive materials and/or a relatively larger and thicker, in terms of wall size, pressure vessels [18]. The low steam temperature decreases the cycle thermal efficiency and increases the risk of damaging steam turbines at part-load operating conditions [19]. Therefore, steam-accumulation TES systems are usually coupled with a superheater to increase the temperature of the discharged saturated steam (i.e., above the saturation temperature) before entering the steam turbine. The superheating process can be performed using: (i) another group of higher temperature and pressure SAs and a superheating heat exchanger; or (ii) higher temperature sensible or latent TES [16].

Prieto et al. [20] compared the thermodynamic and economic performances of the two aforementioned superheating options, in which two tanks of molten salt are employed for the superheating process in the extended configuration. It was concluded that the conventional option is more feasible and more cost-effective than using the combination of SAs and molten-salt tanks for energy storage, especially for storage durations of less than 6 h. It is mainly due to the added complexity, high melting point and high costs of molten-salt storage systems. Furthermore, Bai et al. [21] analysed the thermal characteristics of combining SAs with concrete as superheating storage media, proving the feasibility of this combination. However, the performance of this arrangement was not evaluated in a whole power plant level, and the thermodynamic and economic potential of this combination is not clear yet.

Moreover, several studies proposed and tested different sensible heat and latent TES options for DSG [10,17,22–26], but SAs were not an option in those TES configurations. For example, the use of PCM-based TES systems is suggested by Birnbaum et al. [10] as well as by Guédez et al. [26]. Both studies showed a potential increase of profitability and capacity factors of the studied DSG plants. Furthermore, a study performed by Li et al. [27] suggested the implementation of secondary organic and steam Rankine bottoming cycles to maximise the overall power output from heat stored in SAs. The study also suggested the use of extra low-pressure SA, in addition to the existing high-pressure SA. This extra SA increases the total storage capacity by 360 % comparted to having a high-pressure SA only. It was concluded that adding a secondary power generation system and a low-pressure SA improves the overall cost-effectiveness of the DSG plant.

There are many options for solid-state sensible TES to be considered in the steam accumulator-sensible TES system. These include concrete, cast iron, cast steel and silica fire bricks [28]. However, concrete has proven through testing its capability of high-temperature heat storage (up to 550 °C), its ability to withstand large number of charging/discharging cycles, and its relatively low cost [29–32]. The use of concrete for TES has been already commercially available as revealed by the thermal battery technology developed by EnergyNest [33], approving the validity and applicability to utilise concrete for TES applications.

Nevertheless, all the aforementioned previous research did not compare the thermodynamic performance and the economic returns of operating the two steam-accumulation options in a DSG CSP power plant. Therefore, the present work goes beyond a previous analysis [34] with the aim of performing a comprehensive thermo-economic analysis and comparison of two steam-accumulation options (i.e., with and without the concrete storage) for an existing DSG CSP plant (Khi Solar One in South Africa) during charging and discharging. The main novel contributions of this work include:

- modelling and validation of the power generation cycle of the reference DSG CSP plant in baseload and part-load operating modes, including the analysis of off-design turbine efficiencies;
- modelling and validation of the charging/discharging modes of SAs, including the performance of parametric thermo-economic analysis for a range of initial water filling ratios;
- transient modelling and validation of heat transfer between the steam and the concrete, including the consideration of steam condensation process during charging process;
- parametric analysis of the thermo-economic performance for different sizes of concrete blocks;
- cost estimation of all TES system components using dedicated costing methods; and,
- profitability assessment of the two options for the reference DSG CSP plant at different electricity prices.

The study firstly describes, in Section 2, the layout of the selected DSG CSP plant and the compared TES systems. The modelling methods is presented in Section 3. The thermodynamic and the economic evaluations of the compared TES system configurations are presented in Section 4. Finally, the key findings and conclusions are summarised in Section 5.

Table 1
Khi Solar One solar tower and heliostat field parameters.

Parameter	Symbol	Value
Evaporator efficiency (%)	η_{evp}	92
Evaporator outlet pressure (MPa)	P_{16}	12.3
Evaporator outlet temperature (°C)	T_{16}	330
Superheater efficiency (%)	η_{spr}	85
Superheater outlet pressure (MPa)	P_1	12.0
Superheater outlet temperature (°C)	T_1	530
Total heliostat reflective area (km^2)	A_{total}	0.57
Heliostat efficiency (%)	η_{hel}	97

2. Khi Solar One plant and proposed extension

Khi Solar One, which is a 50-MW DSG solar tower CSP plant in South Africa, is selected as the reference power plant. The main components of Khi Solar One are: (i) a heliostat field; (ii) a solar tower; (iii) a power generation block; and (iv) a TES system. The solar tower has two solar receivers, an evaporator, and a superheater. The evaporator is designed to collect solar heat and evaporate the feedwater coming from the power generation block to a temperature of 327 °C at 12.3 MPa (i.e., saturated vapour). The evaporated steam is then superheated to 530 °C at 12 MPa in the solar superheater. The main parameters of the two solar receivers and the heliostat field are summarised in Table 1. All Khi Solar One design and thermodynamic parameters were provided by the operators of Khi Solar One.

The rate of absorbed heat in the evaporator and in the superheater were calculated using direct normal irradiance (DNI) data:

$$\dot{Q}_{evp} = q_{irr} A_{evp} \eta_{hel} \eta_{evp} \quad (1)$$

$$\dot{Q}_{spr} = q_{irr} A_{spr} \eta_{hel} \eta_{spr} \quad (2)$$

$$A_{total} = A_{evp} + A_{spr} \quad (3)$$

where $\dot{Q}$ is the rate of absorbed heat, q_{irr} the direct normal solar irradiance, A the reflective area, η the efficiency and subscripts 'evp', 'spr', and 'hel' stand for the evaporator, superheater, and heliostat.

As indicated in Equations (1) and (2), the amount of heat depends on the reflective area of the heliostat that is allocated for each receiver. The total heliostat reflective area for both receivers, A_{total}, is assumed to be fixed. However, the fraction of the total area allocated for each receiver (i.e., A_{evp} and A_{spr}) can be varied. This means that if more solar power is required in the evaporator, more reflective area goes to the evaporator, which in turn reduces the reflective area allocated for the superheater as the total reflective area is constant.

The evaporator and the superheater are designed to absorb extra solar thermal power, when available, beside the required amount to generate the 50 MW of electrical power. The excess heat, which can be absorbed during high solar rays (mid-days), is to be stored in the TES system. The stored heat is then utilised for electricity generation during low or no sun times (i.e., night-time). In this study, two TES system configurations are compared. The two configurations are described in detail in Sections 2.1 and 2.2.

2.1. Existing TES configuration with steam accumulators

The schematic diagram of Khi Solar One power plant with its existing TES system is shown in Fig. 1. The existing TES system configuration consists of two groups of SAs, base SAs and superheating SAs, as well as a storage superheater. During normal operation of the power plant with no TES system operations, feedwater flows into the evaporator (Stream 15) and absorbs solar heat until becoming saturated steam at 12.3 MPa. The saturated steam (Stream 16) is then superheated in the solar superheater to 530 °C at 12 MPa and then flows (Stream 1) to the power generation block for electricity generation.

The charging mode takes place when there is excess solar thermal power in the evaporator. In this case, extra feedwater is fed from the condensate storage tank (Stream 21) to the solar evaporator and then

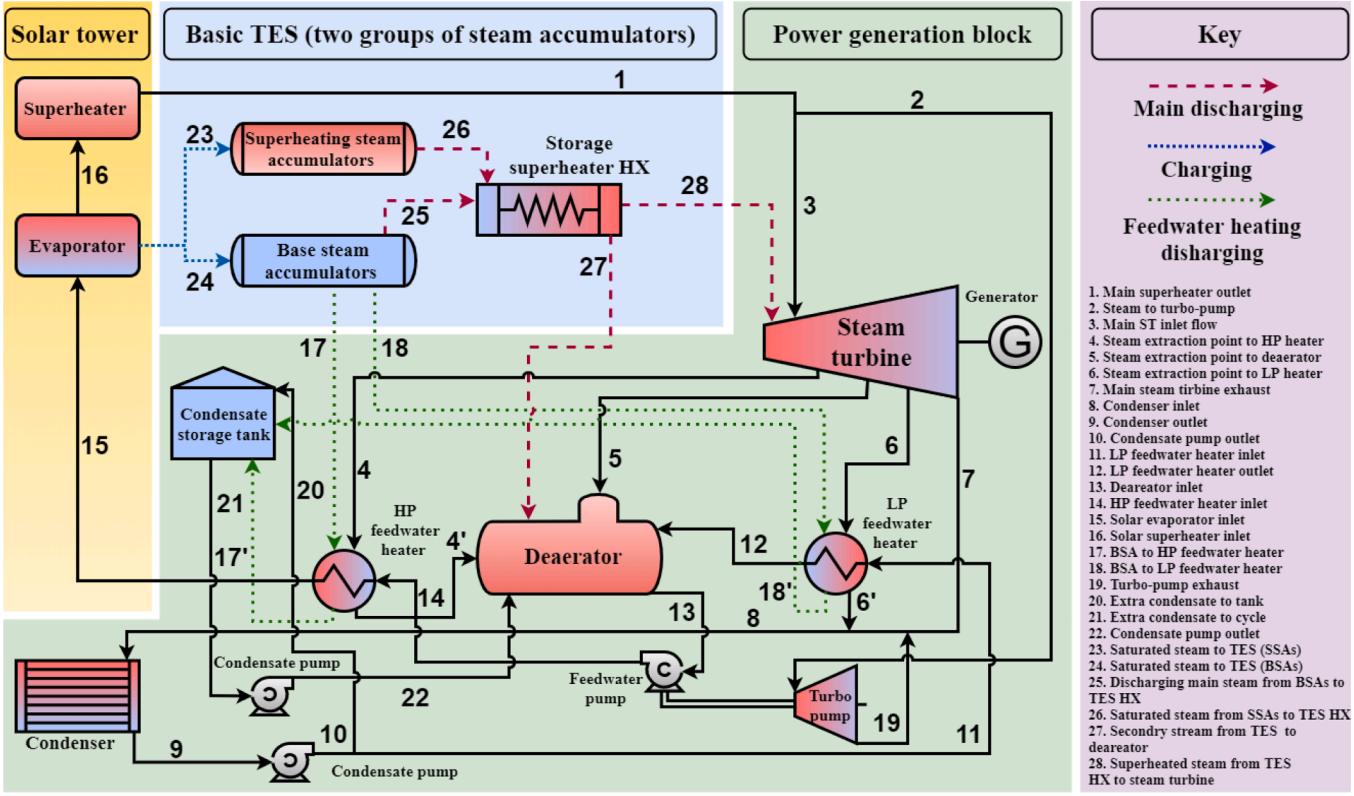

Fig. 1. Schematic diagram of Khi Solar One with the existing TES system configuration (two groups of steam accumulators).

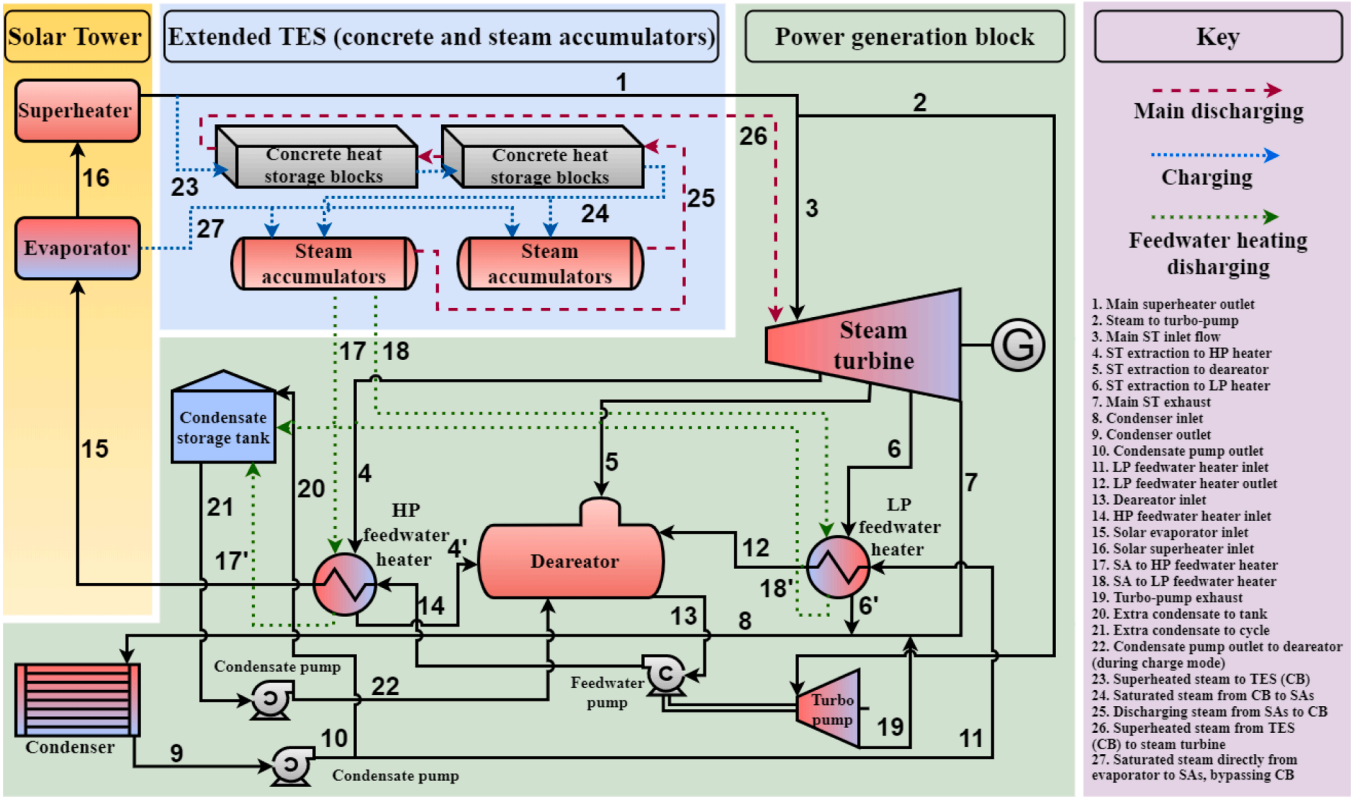

Fig. 2. Schematic diagram of Khi Solar One with the (proposed) extended TES system configuration (concrete blocks and steam accumulators).

directed to the SAs (Streams 23 and 24). The charging process starts first with filling the parallelly connected superheating SAs until reaching the maximum allowable pressure and volume levels and then filling the parallelly connected base SAs, which also stops when reaching the maximum pressure and volume levels set for the base SAs. The size and the thermodynamic limits and constraints for all SAs are discussed in Section 3.2.

There is the option of charging the superheating SAs with superheated steam from the solar superheater at 530 °C and 12 MPa. However, the temperature of the stored water/steam in the SAs can only reach 324 °C (i.e., saturation temperature at 12 MPa). Reaching this temperature and pressure is expected to have a minor enhancement, relative to the concrete blocks option, on the turbine inlet temperature and the cycle efficiency during discharging mode. Additionally, the intention of this study is to use the same SA limits provided by Khi Solar One operators. Thus, the option of increasing the maximum pressure of the superheating SAs to 12 MPa is not considered in this study.

During main discharging process, the base SAs release saturated steam at the storing pressure. The discharged steam flows into the storage superheater (Stream 25), gets superheated by the higher temperature saturated steam (i.e., higher pressure) from the superheating SAs (Stream 26), and then flows into the steam turbine for electricity generation (Stream 28). The superheating process of the saturated steam is essential to avoid creation of water droplets in the steam turbine and to increase the cycle thermal efficiency as well. Discharging mode of the base SAs can also be performed for feedwater heating purposes (Streams 17 and 18) during normal operations of the power plant. The direction of the SA feedwater heating stream is indicated by the green dotted lines in Fig. 1.

2.2. Extended TES configuration with solid storage

A schematic diagram of the extended TES system configuration is shown in Fig. 2. The extended TES system consists of concrete blocks and only one group of SAs. All the other power plant components are the same as in the existing TES system configuration descried in Section 2.1.

The operation of the power plant with the extended TES system during normal mode is similar to that with the existing TES system. However, the charging process of the extended configuration is different. Excess solar heat in the solar tower is not only utilised to evaporate extra amount of water for storage, but also to superheat the steam to 530 °C, the same temperature of the main steam flowing into the steam turbine. The superheated steam (i.e., allocated for storage) flows into the concrete blocks (Stream 23), connected in series, first to deposit its high-temperature heat and then fills the parallelly connected SAs (Stream 24). There is also a direct link between the solar evaporator and the SAs (Stream 27), allowing a direct charging of SAs from the evaporator (i.e., as in the existing configuration) in situations when the temperature of steam exiting the last concrete block is higher than the design temperature of the SAs.

The main discharging mode in the extended TES system is performed by releasing the stored saturated steam in the SAs (Stream 25) to the concrete blocks. The saturated steam gets superheated in the higher-temperature concrete blocks and then flows into the steam turbine (Stream 26) for electricity generation. Unlike the existing configuration, there is no need for two groups of SAs and for a storage superheater as steam is superheated while flowing inside the concrete blocks. Similar to the existing TES system, steam can also be released from the SAs for feedwater heating purposes (Streams 17 and 18).

3. Methods

The power cycle model and key assumptions are described in Section 3.1, and the modelling of the SAs in both TES configurations is presented and discussed in Section 3.2. The formulated model of the concrete TES is described in detail in Section 3.3. The cost assessment and key economic performance indicators are discussed in Section 3.4, and in Section 3.5 the approach taken for the analysis of the DNI data used in this study are stated along with Khi Solar One's operational modes.

Table 2
Main energy and mass balance equations used in the power generation cycle model.

Component	Part	Energy balance equations	Mass balance equations
Solar evaporator		$\dot{Q}_{evp} = \dot{m}_{15}(h_{16} - h_{15})$	$\dot{m}_{15} = \dot{m}_{16} + \dot{m}_{23} + \dot{m}_{24}$
Solar superheater		$\dot{Q}_{spr} = \dot{m}_{16}(h_1 - h_{16})$	$\dot{m}_{16} = \dot{m}_1$
Steam turbine	Part 1	$\dot{W}_{T,P1} = \dot{m}_{T,P1}(h_3 - h_4),\ \eta_{T,P1} = \frac{h_3 - h_4}{h_3 - h_{is,4}}$	$\dot{m}_{T,P1} = \dot{m}_3 = \dot{m}_1 - \dot{m}_2$
	Part 2	$\dot{W}_{T,P2} = \dot{m}_{T,P2}(h_4 - h_5),\ \eta_{T,P2} = \frac{h_4 - h_5}{h_4 - h_{is,5}}$	$\dot{m}_{T,P2} = \dot{m}_{T,P1} - \dot{m}_4$
	Part 3	$\dot{W}_{T,P3} = \dot{m}_{T,P3}(h_5 - h_6),\ \eta_{T,P3} = \frac{h_5 - h_6}{h_5 - h_{is,6}}$	$\dot{m}_{T,P3} = \dot{m}_{T,P2} - \dot{m}_5$
	Part 4	$\dot{W}_{T,P4} = \dot{m}_{T,P4}(h_6 - h_7),\ \eta_{T,P4} = \frac{h_6 - h_7}{h_6 - h_{is,7}}$	$\dot{m}_{T,P4} = \dot{m}_{T,P3} - \dot{m}_6 = \dot{m}_7$
	whole	$\dot{W}_T = \dot{W}_{T,P1} + \dot{W}_{T,P2} + \dot{W}_{T,P3} + \dot{W}_{T,P4}$	
Condenser		$x_9 = 0$	$\dot{m}_8 = \dot{m}_{6'} + \dot{m}_7 + \dot{m}_{19},\ \dot{m}_9 = \dot{m}_8$
Turbo-pump		$\dot{W}_{TP} = \dot{m}_2(h_2 - h_{19}),\ \eta_{TP,is} = \frac{h_2 - h_{19}}{h_2 - h_{is,19}}$	$\dot{m}_2 = \dot{m}_{19}$
LP feedwater heater	cold side	$\dot{Q}_{LFWH} = \dot{m}_{11}(h_{12} - h_{11})$	$\dot{m}_{12} = \dot{m}_{11}$
	hot side	$\dot{Q}_{LFWH} = \dot{m}_6(h_6 - h_{6'})$ or $\dot{Q}_{LFWH} = \dot{m}_{18}(h_{18} - h_{18'})$	$\dot{m}_{6'} = \dot{m}_6$ or $\dot{m}_{18'} = \dot{m}_{18}$
HP feedwater heater	cold side	$\dot{Q}_{HFWH} = \dot{m}_{14}(h_{15} - h_{14})$	$\dot{m}_{15} = \dot{m}_{14}$
	hot side	$\dot{Q}_{HFWH} = \dot{m}_4(h_4 - h_{4'})$ or $\dot{Q}_{HFWH} = \dot{m}_{17}(h_{17} - h_{17'})$	$\dot{m}_{4'} = \dot{m}_4$ or $\dot{m}_{17'} = \dot{m}_{17}$
Condensate pump		$\dot{W}_{CP} = \dot{m}_9(h_{10} - h_9),\ \eta_{CP} = \frac{h_{is,10} - h_9}{h_{10} - h_9}$	$\dot{m}_9 = \dot{m}_{10}$
Feedwater pump		$\dot{W}_{FP} = \dot{m}_{13}(h_{14} - h_{13}),\ \eta_{FP} = \frac{h_{is,14} - h_{13}}{h_{14} - h_{13}}$	$\dot{m}_{14} = \dot{m}_{13}$
Deaerator		$\dot{m}_{13}h_{13} = \dot{m}_{4'}h_{4'} + \dot{m}_5h_5 + \dot{m}_{12}h_{12} + \dot{m}_{22}h_{22}$	$\dot{m}_{13} = \dot{m}_{4'} + \dot{m}_5 + \dot{m}_{12} + \dot{m}_{22}$

Table 3
Main cycle parameters and assumptions used in the power generation cycle model at the full rated electrical power of 50 MW. The data were provided by the operators of Khi Solar One.

Parameter	Symbol	Stream	Value
Turbine inlet temperature (°C)	T_1	1	520
Turbine inlet pressure (MPa)	P_1	1	11.5
Turbine first side extraction pressure (MPa)	P_4	4	2.86
Turbine second side extraction pressure (MPa)	P_5	5	1.27
Turbine third side extraction pressure (MPa)	P_6	6	0.27
Condensing pressure (MPa)	P_7	7	0.018
Condensate pump outlet pressure (MPa)	$P_{10,11}$	10,11	1.34
Feedwater pump outlet pressure (MPa)	P_{14}	14	15.4
LP and HP feedwater heaters pressure loss (MPa)	$\Delta P^{loss}_{LFWH}, \Delta P^{loss}_{HFWH}$	–	0.70
Deaerator pressure loss (MPa)	ΔP^{loss}_{DE}	–	0.57
Solar evaporator pressure loss (MPa)	ΔP^{loss}_{evp}	–	3.1
Solar superheater pressure loss (MPa)	ΔP^{loss}_{spr}	–	0.3
Turbo-pump isentropic efficiency (%)	$\eta_{TP,is}$	–	75
Turbo-pump mechanical efficiency (%)	η_{TP}	–	85
Feedwater pump isentropic efficiency (%)	η_{FP}	–	81
Condensate pump isentropic efficiency (%)	η_{CP}	–	78
Generator mechanical efficiency (%)	η_{gen}	–	94
LP and HP feedwater heaters heat-to-heat efficiency (%)	η_{LFWH}, η_{HFWH}	–	95
Ambient pressure (MPa)	P_a	–	0.1
Ambient temperature (°C)	T_a	–	28

3.1. Power cycle model and assumptions

The power generation block of Khi Solar One, illustrated in Figs. 1 and 2, consists of the following:

- a 50-MW steam turbine driving an electric generator, fitted with three side steam extractions for feedwater heating;
- low-pressure (LP) and high-pressure (HP) closed feedwater heaters, which are supplied by steam from the turbine side extraction points or from the SAs;
- a deaerator that works as an open feedwater heater and maintains the oxygen and other dissolved gases levels below the maximum limits;
- a feedwater pump that is operated by a separate turbo-pump and two condensate pumps;
- a condensate storage tank that stores water at ambient temperature and pressure; and,
- a natural draft condenser to maintain the vacuum at the steam turbine outlet and to condensate the exhaust steam leaving the turbine.

The energy and mass balance equations written for each component, and which were solved to predict the performance of the power generation block (i.e., steam Rankine cycle), are summarised in Table 2. All steam cycle modelling tasks and simulations were performed using MATLAB [35] and all steam thermodynamic properties were obtained from REFPROP interface [36].

Table 4
Isentropic efficiencies of turbine parts at design and off-design operating conditions.

Turbine part number	Design-point efficiency (%)	Off-design efficiency (%)
1	84	82
2	86	85
3	90	87
4	78	76

Table 5
Main SA parameters and constraints in the analysed TES system configurations.

Parameter	Existing		Extended
	Superheating SAs	Base SAs	All SAs
Number of SAs (units)	3	16	19
Useful volume/unit (m^3)	197	197	197
Maximum pressure (MPa)	8.2	4.2	8.2
Minimum pressure (MPa)	3.9	1.4	1.9
Maximum WFR (-)	0.99	0.99	0.99

The net generated power and net thermal efficiency during nominal operation mode ($\eta_{Cyc,nom}$), charging mode ($\eta_{Cyc,Ch}$) and discharging mode ($\eta_{Cyc,Dch}$) of the plant were calculated from:

$$\dot{W}_{net} = \eta_{gen} \sum \dot{W}_T - \sum \dot{W}_P \tag{4}$$

$$\dot{Q}_{ST\rightarrow Cyc} = \dot{m}_{Cyc}\,(h_1 - h_{15}) \tag{5}$$

$$\dot{Q}_{ST\rightarrow TES} = \dot{m}_{TES}\,(h_{23} - h_{15}) \tag{6}$$

$$\dot{Q}_{ST} = \dot{Q}_{eva} + \dot{Q}_{spr} \tag{7}$$

$$\dot{Q}_{ST} = \dot{Q}_{ST\rightarrow Cyc} + \dot{Q}_{ST\rightarrow TES} \tag{8}$$

$$\Delta\dot{Q}_{TES} = \dot{Q}_{TES\rightarrow Cyc} - \dot{Q}_{Cyc\rightarrow TES} \tag{9}$$

$$\eta_{Cyc,nom} = \frac{\dot{W}_{net}}{\dot{Q}_{ST\rightarrow Cyc}} \tag{10}$$

$$\eta_{Cyc,Ch} = \frac{\dot{W}_{net}}{\dot{Q}_{ST\rightarrow Cyc} + \Delta\dot{Q}_{TES}} \tag{11}$$

$$\eta_{Cyc,Dch} = \frac{\dot{W}_{net}}{\dot{Q}_{TES\rightarrow Cyc}} \tag{12}$$

where $\dot{W}_T$ is the turbine power output, $\dot{W}_p$ the power needed by each pump, $\dot{Q}_{ST\rightarrow Cyc}$ the rate of heat from the solar tower to the cycle, $\dot{Q}_{ST\rightarrow TES}$ the rate of heat from the solar tower to the TES system, $\dot{Q}_{TES\rightarrow Cyc}$ the rate of heat from the TES system to the cycle, $\dot{Q}_{Cyc\rightarrow TES}$ the rate of heat from the cycle to the TES system, $\dot{Q}_{ST}$ the rate of absorbed heat in the solar tower, $\Delta\dot{Q}_{TES}$ the net rate of heat added to or extracted from the TES system, η the efficiency and subscripts 'nom', 'gen', 'Cyc', 'Ch', and 'Dch' stand for nominal, generator, cycle, charging and discharging, respectively.

The main assumptions used in the quasi-steady power generation cycle model include:

- 10 °C $\leq \Delta T_{LM}$ in both the LP and HP feedwater heaters;
- 10 °C $\leq \Delta T_{pp}$ of the inlet and the outlet of both HP and LP feedwater heaters [37];
- all pump suction pressures are adjusted and controlled to avoid pump cavitation [38,39];
- no mass loss across all power cycle components; and,
- all feedwater heaters are equipped with steam traps so that saturated liquid is collected through throttling and flows into the deaerator/condenser units [40,41].

All other parameters including component efficiencies, pressure losses, etc., are listed in Table 3.

The assumed turbine isentropic efficiency for each turbine part during nominal (design) and part-load (off-design) operation conditions are listed in Table 4. The turbine is divided into 4 parts. Each part is defined as a group of turbine stages and each stage consists of a stator and a rotor. Turbine Part 1 includes the stages between the turbine inlet and first side extraction, Part 2 represents the stages between the first and second side extractions, Part 3 includes the stages between the second and third side extractions, and Part 4 represents the stages between the third side extraction and main outlet. The efficiencies were assumed after comparing off-design efficiency data (provided by Khi Solar One operators) with correlations for the estimation of off-design turbine efficiencies from Refs. [42,43]. This analysis demonstrates that using the average value of the provided off-design efficiencies for each turbine part is a reasonable choice, as it is associated with the lowest discrepancy (root mean square error, RMSE < 0.1) between the provided and correlation-based data for all examined off-design conditions.

3.2. Steam accumulator model

All SAs in both TES systems (i.e., existing and extended) were thermodynamically modelled using the mass and the energy balance equations of the thermal equilibrium model developed by Stevanovic et al. [44], which are explained in detail in Appendix A. The two main equations (i.e., derivation can be found in Appendix A) for predicting the mass of water/steam and the pressure of the steam in the SAs are:

$$\frac{dm}{dt} = \Delta\dot{m}_V + \Delta\dot{m}_L \tag{13}$$

$$\frac{dP}{dt} = \frac{\Delta(\dot{m}h)_V + \Delta(\dot{m}h)_L + \left(\frac{\Delta h_{vap}\frac{V}{m}}{\nu''-\nu'} - h\right)(\Delta\dot{m}_V + \Delta\dot{m}_L)}{m\left(\frac{dh'}{dP} + \frac{\frac{V}{m}-\nu'}{\nu''-\nu'}\frac{d\Delta h_{vap}}{dP} - \frac{\Delta h_{vap}}{\nu''-\nu'} - \frac{d\nu'}{dP} - \Delta h_{vap}\frac{\frac{V}{m}-\nu'}{(\nu''-\nu')^2}\frac{d(\nu''-\nu')}{dP}\right) - V} \tag{14}$$

where P is the SA pressure, m the mass of steam/water in the SA, V the SA volume, Δh_{vap} the latent heat of vaporisation, ν the specific volume, and superscripts 'V', 'L', '′' and '″' stand for liquid, vapour, saturated liquid, and saturated vapour conditions, respectively.

Equations (13) and (14) were solved numerically using the explicit fourth- and fifth-order Runge-Kutta method, known as Dormand-Prince pair, (i.e., solver *ode45* in MATLAB [45]) for specified initial values of SA water/steam mass and pressure. Moreover, the steam thermodynamic properties presented in Equation (14) are only a function of pressure. Therefore, their rates of change were calculated using the slope of the property between slightly higher and lower pressure points.

3.2.1. Validation of the steam accumulator model

The validation of the formulated SA model was conducted using a set of data for three different SA charging and discharging tests reported in Ref. [44]. The details of the tests and the validation results are summarised in Appendix A. Overall, the formulated model can be considered as sufficiently accurate because the maximum RMSE and the maximum average relative error (ϵ_{avg}) between the simulation results and the reported data of the validation tests are 0.05 and 1.4 %, respectively.

3.2.2. Initial conditions and constraints

The main parameters of the SAs in the compared TES system configurations are summarised in Table 5. For the existing TES system, the maximum and the minimum pressures were selected based on operational data provided by the plant operators. The superheating SAs are charged to a higher pressure due to the need of having a higher temperature discharging

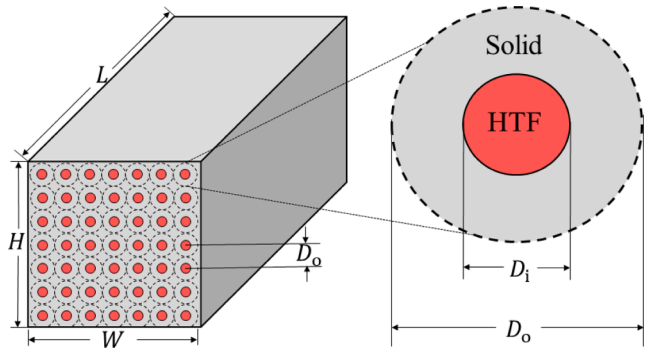

Fig. 3. Simplified schematic diagram of a concrete storage block with in-line tube bundle arrangement. The right sketch shows the radial cross section of one HTF-solid (steam-concrete) element.

steam (i.e., higher saturation pressure) for the superheating process during the discharging mode. The minimum pressure of the base SAs was selected based on the lowest pressure the steam turbine can accept. In the extended TES system, the minimum was set by considering a 0.5 MPa pressure loss through the concrete blocks before entering the turbine. The maximum pressure for all SAs is the same since the superheating process undergoes in the concrete blocks. All SAs are also constrained with water filling ratios (WFR) of 0.99. The WFR is defined as:

$$WFR = \frac{V_L}{V_V + V_L} = \frac{V_L}{V_{SA}} \tag{15}$$

where V_L is the liquid volume, V_V the vapour volume and V_{SA} the volume of the SA.

The maximum inlet (i.e., charging) steam temperature and pressure of all SAs in both TES systems are 327 °C and 12 MPa, respectively, which is set by materials limits. The SA external surfaces are assumed to be perfectly insulated, hence, there is no heat loss to the environment.

3.3. Concrete thermal energy storage model

In this work, concrete is selected as the storage material because it has proven its compatibility of storing heat at high temperatures (up to 550 °C) and its comparatively cheaper price [29]. The schematic diagram of the proposed concrete blocks and the tube bundling is illustrated in Fig. 3. Each concrete block is assumed to be 10-m long and to have a square cross-section for easier installation and operation near the SAs, and each is assumed to comprise a number of tubes that are surrounded by concrete. The inner and outer diameters of each tube-solid element, D_i and D_o as shown in Fig. 3, are equal to 2 cm and 8 cm [46,47]. The total size of the concrete blocks (i.e., width, height, length) is determined after performing a thermo-economic parametric study for different concrete block sizes (i.e., in terms of number of tubes and number of concrete blocks) in Section 4.3.1.

In this study, a transient energy and mass balance model was formulated based on the following assumptions:

- Conductive axial heat transfer within the fluid and between each solid element is very small compared to the radial heat transfer (i.e., $\dot{Q}_{axial} \ll \dot{Q}_{radial}$). The ratio of the maximum axial to the minimum radial heat transfer rates ($\dot{Q}_{axial,max}/\dot{Q}_{radial,min}$) is less than 0.5 %. Thus, conductive axial heat transfer is neglected.
- The external surface of the concrete block is perfectly insulated (i.e., no heat loss to the environment).
- The transient radial heat conduction in the solid element is treated using a modified lumped capacitance method with an effective heat transfer coefficient (i.e., valid for large Biot numbers, up to 100) that accounts for the internal thermal gradient in the solid material [48,49].
- The tube between the solid and the fluid is very thin and made of a material that has a relatively high thermal conductivity(34–54 W/m K for carbon steel [50,51]), which is at least 15 times greater than the thermal conductivity of concrete (2.2 W/m K at 200 °C [52]). Based on the dimensions of the solid element and the tubes (thickness of 1 mm [49]), the calculated thermal resistance of the tube was observed to be less than 1 % of that of the solid element. Therefore, the thermal resistance of the tube is neglected.
- Steam condensation is expected to occur during charging mode. Therefore, the two phases (vapour and liquid) are assumed to be in thermal, mechanical, and chemical equilibrium.
- Fluid flow is one dimensional (z-axis) and the velocity vector of each phase of the fluid (liquid and vapour) has one component only.
- Pressure drop of fluid in the tube is neglected when calculating fluid properties. However, a total pressure loss of 0.5 MPa throughout the concrete blocks is assumed.
- Temperature distribution in the solid is symmetrical about the axis.

Applying the listed assumptions and using the general energy and mass balance equations for unsteady-flow processes in Ref. [41], the final energy and mass balance equations for the fluid element can be written as:

$$\frac{d(m_f u_f)}{dt} = \dot{m}_{f,in} h_{f,in} - \dot{m}_{f,out} h_{f,out} + \alpha_e A_w (T_s - T_f) \tag{16}$$

$$\frac{dm_f}{dt} = \dot{m}_{f,in} - \dot{m}_{f,out} \tag{17}$$

$$A_w = \pi D_i \Delta z \tag{18}$$

where m_f and u_f are the mass and the specific internal energy of the fluid, respectively, $\dot{m}_f$ the fluid mass flowrate, h_f the fluid specific enthalpy, α_e the effective heat transfer coefficient, A_w the tube surface area, T_s the solid temperature and T_f the fluid temperature.

It should be noted that the fluid mass in each cell is not constant ($dm_f/dt \neq 0$) as the fluid density in each cell varies, especially during condensation. The temporal change of fluid mass contained within the tube array of the concrete blocks is driven by steam condensation. The density difference between vapour steam and condensed liquid dictates that the mass must increase as liquid is accumulating in a fixed volume, which is captured by the mass balance in Equation (17).

The energy balance equation for the solid in each cell is:

$$m_s c_s \frac{dT_s}{dt} = \alpha_e A_w (T_f - T_s) \tag{19}$$

where m_s is the solid mass and c_s the solid specific heat capacity. The solid mass in each cell is assumed to be constant as the solid density is almost constant for the considered temperature range.

The effective heat transfer coefficient in Equations (16) and (19) was calculated using Equation (20) that was proposed by Xu et al. [48] and Jian et al. [49]. This coefficient was derived by applying the lumped capacitance method and is valid for large (up to 100) Biot numbers, $Bi = (\alpha V_s)/(k_s A)$, and for transient models. Based on a brief numerical analysis, the Biot number in the model is expected to fall between 0.80 and 88 depending on the HTF mass flowrate and the inner and outer diameters of the HTF-solid element.

$$\frac{1}{\alpha_e} = \frac{1}{\alpha_f} + \frac{1}{k_s}\left(\frac{4 R_i R_o^4 \ln\left(\frac{R_o}{R_i}\right) - 3 R_i R_o^4 + 4 R_i^3 R_o^2 - R_i^5}{4 \left(R_o^2 - R_i^2\right)^2} \right) \tag{20}$$

In Equation (20), α_f is the convective heat transfer coefficient of the fluid and calculated using Gnielinski's correlation for single-phase flows [53]:

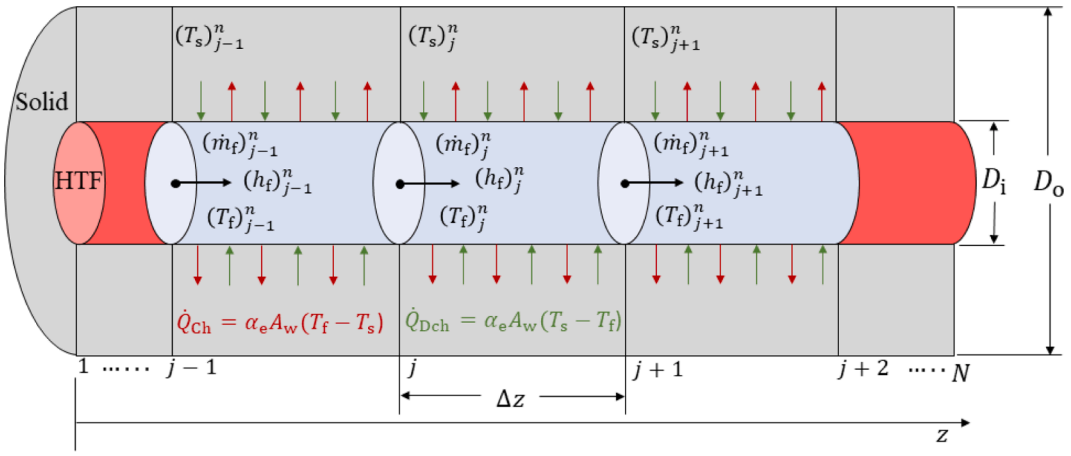

Fig. 4. Schematic diagram of the cell energy and mass balance analysis as well as the heat flow directions during charging and discharging modes.

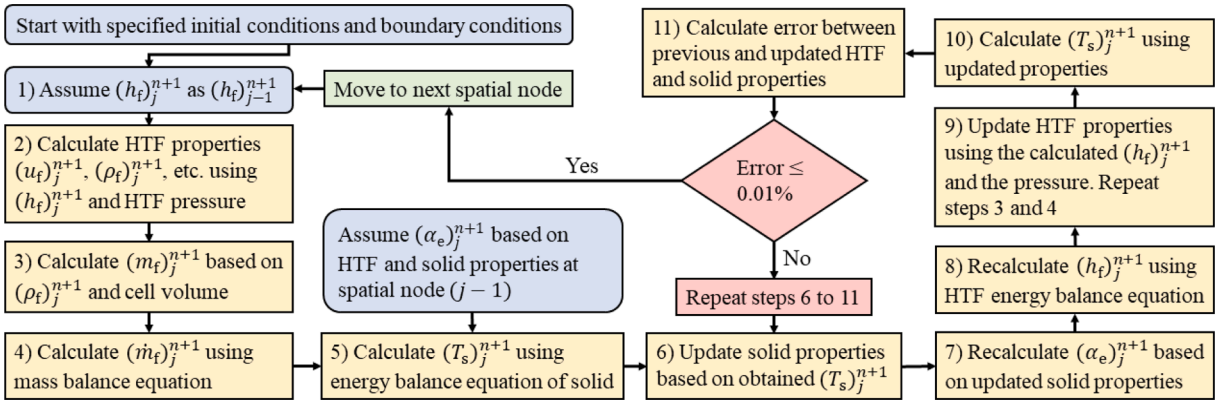

Fig. 5. Flow diagram of the calculation steps of solving the energy and mass balance resolution algorithm for the concrete model. The steps are repeated for each spatial node ($j = 2$ to N) and for each time step, Δt.

Table 6
Thermophysical properties of the selected concrete material (*HEATCRETE vp1*). The unit of temperature in the correlations is °C [52].

Thermophysical property	Value/correlation
Density (kg/m^3)	2260
Thermal conductivity (W/m K)	k_s = -0.0027T + 2.754
Specific heat capacity (J/kg K)	c_s = 1.3192T + 775

$$\alpha_{SP} = \frac{k_f}{D_h} \frac{\left(\frac{f}{8}\right)(Re - 1000)Pr}{1 + 12.7\left(\frac{f}{8}\right)^{0.5}(Pr^{0.67} - 1)} \tag{21}$$

where k_f is the fluid thermal conductivity, Re the Reynolds number, Pr the Prandtl number and f the friction factor that was calculated using Colebrook-White correlation with an absolute tube roughness, e, equal to 0.04 mm for new carbon-steel tubes [54]:

$$\frac{1}{\sqrt{f}} = -2\log\left(\frac{e}{3.7\,D_i} + \frac{2.51}{Re\sqrt{f}}\right) \tag{22}$$

For steam condensation, the fluid heat transfer coefficient was obtained using Shah's correlation for two-phase flows [55,56]:

$$\alpha_{TP} = \begin{cases} \alpha_{Sh} & J_V \geq 0.98(Z + 0.263)^{-0.62} \\ \alpha_{Sh} + \alpha_{Nu} & 0.95\left(1.254 + 2.27Z^{1.249}\right)^{-1} \leq J_V < 0.98(Z + 0.263)^{-0.62} \\ \alpha_{Nu} & J_V < 0.95\left(1.254 + 2.27Z^{1.249}\right)^{-1} \end{cases} \tag{23}$$

$$\alpha_{Sh} = \frac{k_L}{D_h} 0.023\, Re_{Lo}^{0.8} Pr_L^{0.4} \left(\frac{\mu_L}{14\mu_V}\right)^{(0.0058 + 0.557P_R)} \left(1 + \frac{3.8}{Z^{0.95}}\right) \tag{24}$$

$$\alpha_{Nu} = \frac{k_L}{D_h} 1.32\, Re_L^{-1/3} \left(\frac{\rho_L(\rho_L - \rho_V)gk_L^3}{\mu_L^2}\right)^{1/3} \tag{25}$$

$$J_V = \frac{xG}{\left(gD_h\rho_V(\rho_L - \rho_V)\right)^{0.5}} \tag{26}$$

$$Z = \left(\frac{1}{x} - 1\right)^{0.8} P_R^{0.4} \tag{27}$$

$$P_R = \frac{P_{sat}}{P_{crit}} \tag{28}$$

The transient energy and mass balance equations of the fluid and the solid elements were solved numerically using the finite difference method by discretising the total tube length, L, into small spatial segments, Δz, and the total time, τ, into small time steps, Δt. The spatial discretisation and the location of the nodes are illustrated in Fig. 4. This set of equations were solved using the backward Euler:

Table 7
Main correlations and constants used in capital cost estimation of the existing TES system.

Method	Steam accumulator	Heat exchanger (superheater)
General equations	$C_{BM,SA} = F_{BM,SA}\,C_{P,SA}$	$C_{BM,HX} = F_{BM,HX}\,C_{P,HX}$
Seider et al. [57] method	$C_{P,SA} = F_M\,C_{SA} + C_{PL}$ $C_{SA} = \exp\left(5.63 + 0.46(\ln W) + 0.006(\ln W)^2\right)$ $C_{PL} = 2275\,(D_{SA})^{0.2094}$ $F_M = 1.7$ $F_{BM,SA} = 3.05$	$C_{P,HX} = F_{P,HX}F_M F_L\,C_{OB}$ $F_{P,HX} = 0.98 + 0.018\left(\frac{P_{HX}}{100}\right) + 0.0017\left(\frac{P_{HX}}{100}\right)^2$ $F_M = 2.7 + \left(\frac{A_{s,HX}}{100}\right)^{0.07}$ $F_L = 1.0$ $C_{OB} = \exp\left(11.55 - 0.92\,(\ln A_{s,HX}) + 0.098(\ln A_{s,HX})^2\right)$ $F_{BM,HX} = 3.17$
Turton et al. [59] method	$\log C_{P,SA} = 3.56 + 0.38(\log V_{SA}) + 0.091(\log V_{SA})^2$ $F_{BM,SA} = B_1 + B_2 F_M F_{P,SA}$ $F_{P,SA} = \frac{1}{0.0063}\left(\frac{(P_{SA}+1)D_{SA}}{2\,(850 - 0.6\,(P_{SA}+1))} + 0.0032\right)$ $B_1 = 1.49$ $B_2 = 1.52$ $F_M = 1.75$	$\log C_{P,HX} = 4.19 - 0.25\,(\log A_{s,HX}) + 0.197\,(\log A_{s,HX})^2$ $F_{BM,HX} = B_1 + B_2 F_M F_{P,HX}$ $B_1 = 1.63$ $B_2 = 1.66$ $F_M = 2.75$ $\log F_{P,HX} = 0.039 - 0.113\,(\log P_{HX}) + 0.082\,(\log P_{HX})^2$
Couper et al. [60] method	$C_{P,SA} = F_M\,C_{SA} + C_{PL}$ $C_{SA} = 1.67\exp\left(8.57 + 0.23\,(\ln W) + 0.043\,(\ln W)^2\right)$ $C_{PL} = 2291\,(D_{SA})^{0.2029}$ $F_M = 1.7$ $F_{BM,SA} = 1.7$	$C_{P,HX} = 1.218\,F_P F_M F_D\,C_{OB}$ $F_P = 1.14 + 0.121\,(\ln A_{s,HX})$ $F_M = 0.86 + 0.23(\ln A_{s,HX})$ $F_D = \exp(-0.92 + 0.083\,(\ln A_{s,HX}))$ $C_{OB} = \exp\left(8.82 - 0.31\,(\ln A_{s,HX}) + 0.068(\ln A_{s,HX})^2\right)$ $F_{BM,HX} = 1.9$
Ulrich et al. [61] method	$C_{P,SA} = 75000$ $F_M = 2.5$ $F_P = 6$ $F_{BM,SA} = 1.47F_M F_P + 1.55$	$C_{P,HX} = 9000$ $F_M = 3.0$ $F_P = 1.2$ $F_{BM,HX} = 1.5F_M F_P + 1.5$

$$\frac{(m_f u_f)_j^{n+1} - (m_f u_f)_j^n}{\Delta t} = \left(\dot{m}_f\right)_{j-1}^{n+1}(h_f)_{j-1}^{n+1} - \left(\dot{m}_f\right)_j^{n+1}(h_f)_j^{n+1} + (\alpha_e)_j^{n+1}A_w\left((T_s)_j^{n+1} - (T_f)_j^{n+1}\right) \tag{29}$$

$$\frac{(m_f)_j^{n+1} - (m_f)_j^n}{\Delta t} = \left(\dot{m}_f\right)_{j-1}^{n+1} - \left(\dot{m}_f\right)_j^{n+1} \tag{30}$$

$$m_s c_s \frac{(T_s)_j^{n+1} - (T_s)_j^n}{\Delta t} = (\alpha_e)_j^{n+1}A_w\left((T_f)_j^{n+1} - (T_s)_j^{n+1}\right) \tag{31}$$

where n is the time step index and j the spatial node.

In addition to the energy and mass balance equations, fluid properties were obtained from the National Institute of Standards and Technology (NIST) database using the REFPROP interface (more information in Ref. [36]). The equations were solved using an iterative method and following the illustrated algorithm in Fig. 5, with $\Delta t = 1$ s and $\Delta z = 0.1$ m. The time step size was selected after comparing the RMSEs for a range of time step sizes and $\Delta t = 1$ s gives an acceptable amount of uncertainty (0.2 %) and reasonable computational time. Moreover, the model assumed a homogenous starting point where the temperature of fluid in each spatial node was the same as the temperature of the solid and the initial conditions of each calculation step were determined based on previous time step [29]. The cut-off charging and discharging HTF temperatures (Streams 24 and 25 on Fig. 2) were set, respectively, at 327 °C and 212 °C. The first is the design temperature of the SAs and the second is the steam saturation temperature at the minimum SAs pressure (1.9 MPa).

Table 8
Physical properties and dimensions of a single unit of steam accumulator and of the shell and tube (U-shaped) heat exchanger (superheater).

Parameter	Symbol	Steam accumulator	Heat exchanger (superheater)
Unit weight (tons)	W	248	–
Internal diameter (m)	D_{SA}	3.74	–
Volume (m^3)	V_{SA}	247	–
Length (m)	L_{SA}	22.2	–
Design pressure (MPa)	P_{SA}, P_{HX}	13.1	8.2
Tube length (m)	$L_{tube,HX}$	–	>15
Total surface area (m^2)	$A_{s,HX}$	–	60.4
Design material	–	Stainless steel 304	Stainless steel 316

3.3.1. Concrete thermophysical properties

The selected concrete material is *HEATCRETE vp1* that was developed by *EnergyNest* and *HeidelbergCement*. *HEATCRETE vp1* is specially made for TES purposes and could withstand heat of up to 550 °C [33,52]. The thermophysical properties of this material are summarised in Table 6. The properties are temperature dependent, hence, correlations based on temperature were extracted from data in Ref. [52]. The density is also temperature dependent but the change in density is less than 1 % between 200 °C and 550 °C. Thus, an average density of 2260 kg/m^3 was assumed in the whole temperature range.

3.3.2. Validation of the concrete thermal energy storage model

The formulated concrete storage computational model was validated using experimental data from Ref. [49]. The details of the experimental data and the model validation results are summarised and discussed in Appendix B. Overall, the RMSEs of all compared data are 1 or less, and the behaviour of the numerically calculated HTF and solid temperatures are almost the same as the experimental temperatures. Therefore, the formulated model is sufficiently accurate in predicting the performance

Table 9
Costing parameters for concrete blocks.

Components	Symbol	Cost	Reference
Direct costs ($)	$C_{P,CB,total}$	–	
Concrete mixture ($/m^3)	U_C	230	[62]
Tube material – carbon steel ($k/m^3)	U_{tubes}	17	[47]
Insulation ($/m^2)	U_{Ins}	290	[63–65]
Foundation ($/m^2)	U_F	2200	[63–65]
Platform and steel ($/m^2)	$U_{P\&S}$	490	[63,65]
Interconnecting piping and valves (-)	$F_{P\&V}$	0.1	Assumed
Electrical (-)	F_E	0.1	Assumed
Instrumentation and control (-)	$F_{I\&C}$	0.1	Assumed
Indirect costs (-)	$F_{BM,CB}$	1.5	[58]

Table 10
Economic analysis assumptions [68].

Parameter	Symbol	Value
Operation & maintenance costs ($/MWh)	*O&M*	12
Availability factor (%)	F_{ava}	98
Lifetime of the system (years)	n	25
Discount rate (%)	r	10

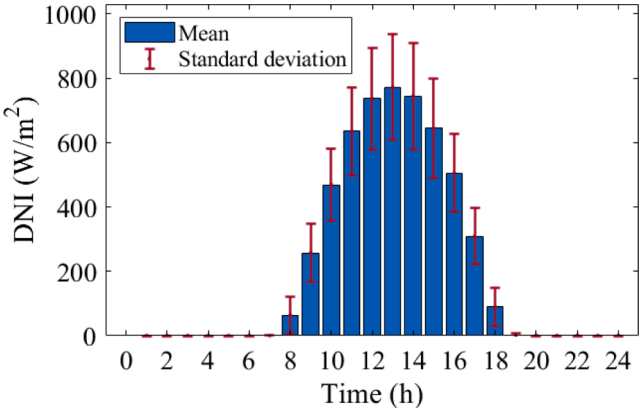

Fig. 6. Mean and standard deviation of the hourly averaged DNI data for a whole year in Upington, South Africa.

of the concrete TES during charging and discharging in this study.

3.4. Cost assessments

The costing of both TES systems is challenging and can involve uncertainties making it difficult to obtain accurate costs. However, in this study, all cost estimation methods are slightly conservative to account for any associated uncertainties related to currency exchange rate, inflation, industry type, and other economic conditions. This is achieved by adjusting the obtained costs using cost indexes from data collection time (i.e., base time) to the time of the analysis as in the following expression, proposed by Seider et al. [57]:

$$C_A = C_B \left(\frac{I_A}{I_B}\right) \tag{32}$$

where C_B is the costs at data collection time, C_A the cost at analysis time, I_B the cost index at base time and I_A the index in the present year.

The cost indexes are based on the chemical engineering plant cost index (CEPCI). The index in 2021, I_A, is 708 [58] and the values of I_B are given in Sections 3.4.1 and 3.4.2. All costs were calculated in USD ($).

3.4.1. Costing of steam accumulators and storage superheater

The capital cost estimation of SAs and storage superheater was performed using four different costing methods, following: Seider et al. [57], Turton et al. [59], Couper et al. [60] and Ulrich et al. [61]. The final cost was determined by computing the average cost of the four methods. These methods take comprehensive consideration of costing characteristics such as manufacturing material, operating pressure, direct and indirect costs, etc. The main correlations and constants used in these methods are listed in Table 7. Moreover, Table 8 summarises the main SA and superheater design parameters and dimensions (i.e., provided by the plant operators) that were used for cost estimations. The base time cost indexes (I_B) were: 567 (year of 2013) for Seider et al. [57], 394 (year of 2001) for Turton et al. [59], 575 (year of 2008) Couper et al. [60] and 400 (year of 2004) for Ulrich et al. [61] methods.

3.4.2. Costing of concrete storage blocks

There are no costing methods for concrete blocks proposed in the literature. Hence, the capital cost of the concrete blocks was estimated using the costs of its constituent materials (concrete mixture, steel, insulation, foundation, etc.). The purchase cost of all concrete blocks was calculated based on the following expressions:

$$C_{P,CB,total} = N_{CB}(C_{CB,1} + C_{CB,2}) \tag{33}$$

$$C_{CB,1} = V_C U_C + V_{tubes} U_{tubes} + A_{s,CB}(U_{Ins} + U_{P\&S}) + A_{b,CB} U_F \tag{34}$$

$$A_{s,CB} = 2L_{CB}W_{CB} + 2L_{CB}H_{CB} + 2H_{CB}W_{CB} \tag{35}$$

$$A_{b,CB} = 2L_{CB}W_{CB} \tag{36}$$

$$V_C = N_{tubes} D_o^2 L_{CB} \tag{37}$$

$$V_{tubes} = N_{tubes} L_{CB} \frac{\pi}{4}\left((D_i + d_{tubes})^2 - D_i^2\right) \tag{38}$$

$$C_{CB,2} = C_{CB,1}(F_{P\&V} + F_E + F_{I\&C}) \tag{39}$$

where N_{CB} is the number of blocks, V_C the concrete volume, V_{tubes} the tube material volume, $A_{s,CB}$ the concrete block surface area, $A_{b,CB}$ the concrete block base area and other symbols are defined in Table 9.

Table 9 lists the costs of the main components of the concrete blocks and the assumed percentages accounting for indirect costs. The concrete mixture price available in the literature ranges from 124 $/m^3 to 510 $/m^3 depending on the mixture and additives [62]. Thus, the average value of the concrete prices was assumed here. The costs of other materials (i.e., insulation, foundation, platform and steel, etc.) were also taken as the average value from the referenced studies.

Similarly, to account for all indirect capital costs of concrete blocks (i.e., labour, engineering, and contingency), the purchase costs was multiplied by a bare module factor, $F_{BM,CB}$, of 1.5 as indicated in Table 9. Hence, the total capital cost of the concrete blocks was calculated by:

$$C_{BM,CB} = F_{BM,CB}\, C_{P,CB,total} \tag{40}$$

The total capital cost of concrete blocks was also corrected for the year of 2021 using Equation (32) since most unit costs listed in Table 9 were reported in 2010. The I_B for the year of 2010 was 551 [58].

3.4.3. Costs of other components

The costing method explained in previous sections exclude the capital cost of the solar tower and the power generation block. The cost of these main components can be obtained by finding the total capital cost of Khi Solar One. Based on information available on the International Finance Corporation and the European Investment Bank websites, the total capital cost of Khi Solar One was estimated between $400M and $450M [66,67]. Both costs were reported in 2012 and before the completion of the project. Therefore, the higher cost was applied here as it covers the contingency costs that was associated with the project. Moreover, this cost includes the

Table 11
List of main results obtained from the formulated Khi Solar One power generation cycle model at full rated power (i.e., no TES system charging/discharging).

Parameter	Symbol	Value
Rate of heat addition in the solar evaporator (MW)	$\dot{Q}_{evp}$	103
Rate of heat addition in the solar superheater (MW)	$\dot{Q}_{spr}$	47
Inlet LP feedwater heater pinch-point temperature difference (°C)	$\Delta T^{in}_{pp,LFWH}$	13
Outlet LP feedwater heater pinch-point temperature difference (°C)	$\Delta T^{out}_{pp,LFWH}$	62
Inlet HP feedwater heater pinch-point temperature difference (°C)	$\Delta T^{in}_{pp,HFWH}$	99
Outlet HP feedwater heater pinch-point temperature difference (°C)	$\Delta T^{out}_{pp,HFWH}$	66
LP feedwater heater logarithmic mean temperature difference (°C)	$\Delta T_{LM,LFWH}$	31
HP feedwater heater logarithmic mean temperature difference (°C)	$\Delta T_{LM,HFWH}$	81
Net electrical power (MW)	$\dot{W}_{net}$	50
Cycle thermal efficiency (%)	$\eta_{Cyc,nom}$	33

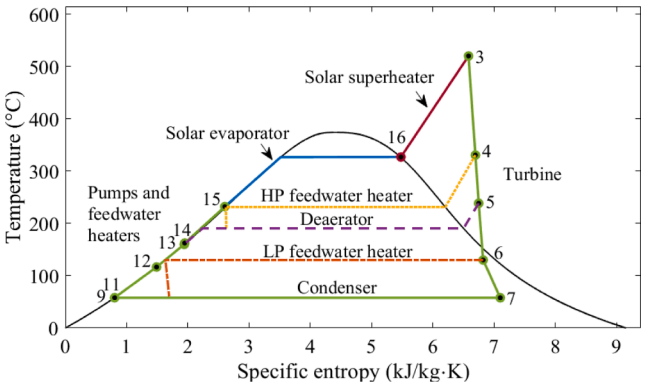

Fig. 7. Temperature-specific entropy (*T-s*) diagram showing the thermodynamic processes of Khi Solar One steam Rankine cycle at full rated power. Each numbered dot represents the thermodynamic state of the numbered flow streams in Figs. 1 and 2.

cost of the existing TES system. Hence, the total capital cost of the power plant without the current TES system was obtained by subtracting the calculated capital costs of the TES system.

3.4.4. Key economic performance indicators

The two TES system configurations are compared using a number of economic performance indicators such as the levelised cost of storage (LCOS) (i.e., cost per kWh of electricity generated utilising stored heat), the levelised cost of electricity (LCOE) and the net present value (NPV), which were calculated using:

$$LCOS = \frac{\sum_{t=1}^{n} \frac{C_{TES,1}+O\&M_{TES,t}}{(1+r)^t}}{\sum_{t=1}^{n} \frac{DE_{TES,t}}{(1+r)^t}} \quad (41)$$

$$LCOE = \frac{\sum_{t=1}^{n} \frac{C_1+O\&M_t}{(1+r)^t}}{\sum_{t=1}^{n} \frac{DE_t}{(1+r)^t}} \quad (42)$$

$$DE_t = F_{ava} \sum_{1}^{365} DE_{day} \quad (43)$$

$$NPV = \sum_{t=1}^{n} \frac{I_t}{(1+r)^t} - \sum_{t=1}^{n} \frac{C_1 + O\&M_t}{(1+r)^t} \quad (44)$$

where C_1 is the capital cost of the power plant components at the first year, $O\&M_t$ the operation and maintenance cost per year, I_t the total revenue per year, DE_t the total amount of discharged electricity per year, subscript 'TES' refers to TES system components only and other symbols are defined in Table 10.

The assumptions listed in Table 10 and the daily mean 24-h DNI profile in Fig. 6 were taken for the calculation of the key economic performance indicators.

Moreover, the internal rate of return (IRR) was also calculated to assess the economic feasibility of investing in the proposed TES configuration. The economic analysis excludes the land, taxation, and financing costs. The electricity generated from Khi Solar One is being sold to the South African Electricity Public Utility (Eskom) under a long-term power purchase agreement (PPA) at a fixed electricity price. However, the price was not declared, perhaps for confidentiality reasons, but it could be around 200 $/MWh as estimated by the South African Energy Department for CSP plants [69]. As the actual price was not provided, the calculations of the NPVs and the IRRs were performed using a range of historical electricity prices, from 100 $/MWh to 340 $/MWh.

3.5. Analysis of DNI data and modes of operation

In order to assess the hourly performance of Khi Solar One with both TES systems, it is essential to have representative hourly averaged DNI data. Therefore, hourly averaged DNI data for a whole year were generated using Meteonorm in TRNSYS [70], taking Upington in South Africa as the location. Running the power plant simulation model for the whole year (i.e., 8760 h) is time consuming. Thus, the DNI data were analysed to create a valid 24-h DNI profile that captures, to some extent, the anticipated behaviour of a year-long DNI in Upington. The analysis included calculating the mean and the standard deviation of the hourly DNI data for a whole year as shown in Fig. 6.

Yet, adapting the mean 24-h DNI profile for the comparative study might not capture the performance of the TES systems during a highly fluctuating DNI profile, a lower DNI profile, or a higher DNI profile. Therefore, the simulation model was also examined for two different 24-h DNI profiles, which are:

- *Profile 1*: mean plus one standard deviation of the DNI data of the whole year; and,
- *Profile 2*: mean minus one standard deviation of the DNI data of the whole year.

The power generation cycle system is assumed to operate with a maximum and a minimum electricity generation of 50 MW and 10 MW, respectively. In this study, it is assumed that Khi Solar One is operated under the following modes:

- *Mode 1:* Electricity is generated at 50 MW or less by utilising thermal power in the solar tower receivers only and no TES charging/discharging is taking place.
- *Mode 2:* Electricity is generated at 50 MW and charging of TES system is performed when excess solar heat is available for storage.
- *Mode 3:* Main thermal power provided by the solar tower receivers and feedwater heating is provided by the SAs in the TES system.

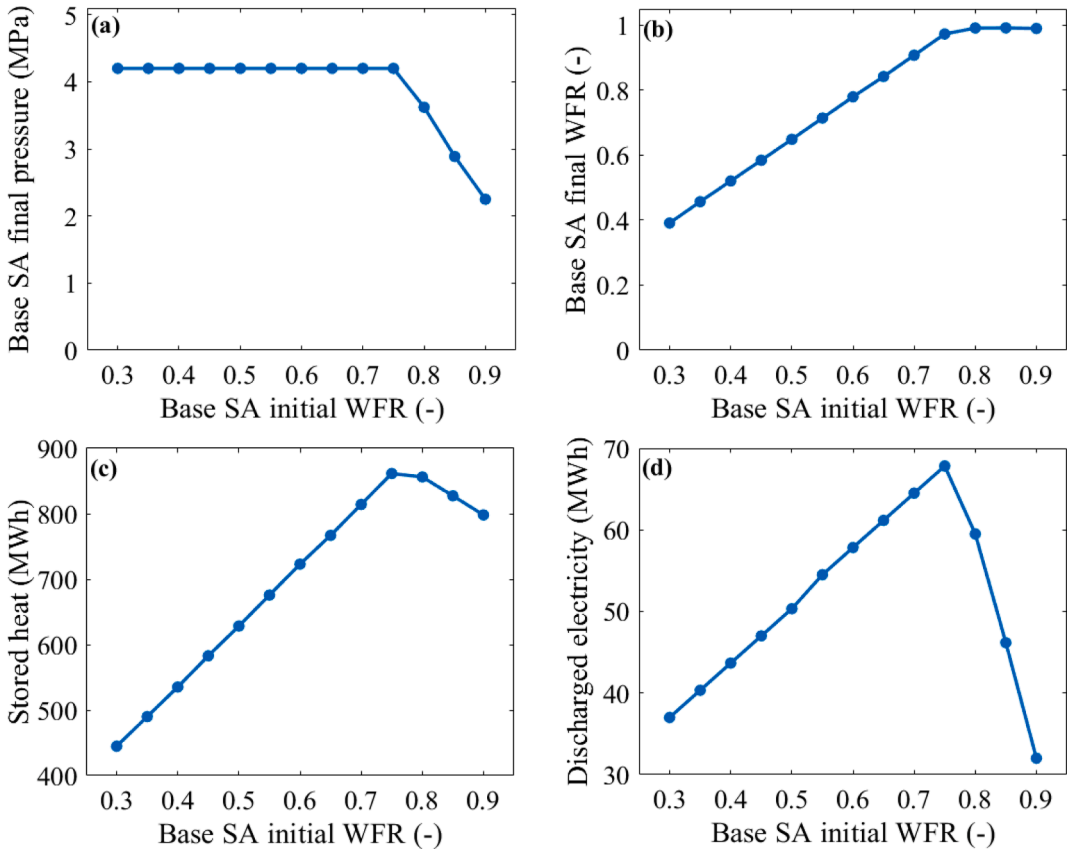

Fig. 8. Effect of different base SA initial WFR on: (a) final pressure of base SAs, (b) final WFR of base SAs, (c) amount of stored heat in the TES system, and (d) amount of discharged electricity utilising the stored heat in the TES system. The initial WFR of the superheating SA group is fixed at 0.5 for all examined cases.

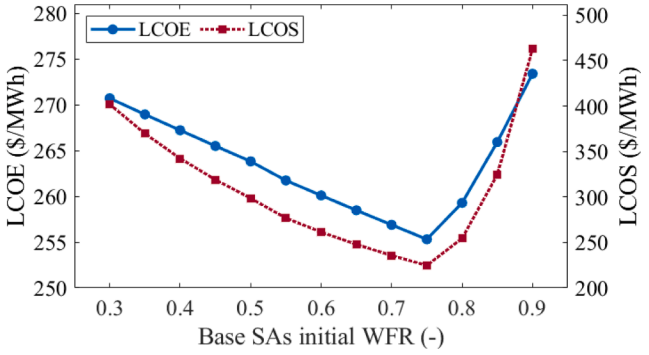

Fig. 9. LCOE and LCOS of Khi Solar One with the existing TES system for the examined range of initial WFRs of the base SAs.

- *Mode 4:* Thermal power is discharged from the TES system to generate 50 MW of electrical power. The TES discharging mode is assumed to start immediately if no thermal power is available in the solar tower.

4. Results and discussion

The obtained results and main findings are presented and discussed in this section. The analysis starts by investigating the operation of Khi Solar One at full rated power without TES. Then, operation of the plant with the existing TES system is investigated in Section 4.2. In Section 4.3, the sizing of concrete blocks and operation One with the extended TES configuration are discussed. Finally, a detailed thermo-economic comparison between the two TES systems is performed in Section 4.4.

4.1. *Khi Solar One at full rated power*

The key results obtained from the formulated Khi Solar One power generation cycle model at full rated (i.e., nominal) power without the operation of the TES system are summarised in Table 11. During this mode, the solar-tower receivers supply 150 MW of thermal power to evaporate and then superheat the subcooled water from 232 °C to 530 °C. About 69 % of this thermal power is provided by the solar evaporator while the remaining, 31 %, is supplied by the solar superheater.

The temperature-specific entropy (*T-s*) diagram showing the main thermodynamic processes of the steam Rankine cycle at nominal load is shown in Fig. 7. The numbered dots in Fig. 7 corresponds to the numbered flow streams indicated in Figs. 1 and 2. The heat addition

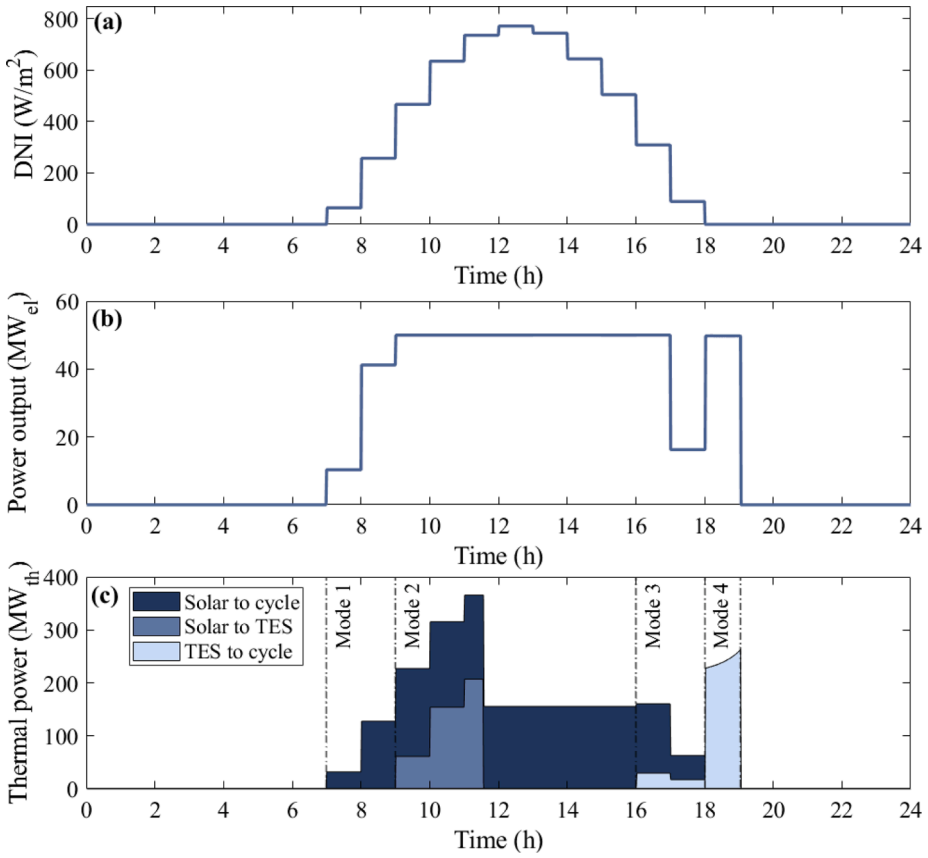

Fig. 10. Diurnal (24-h) performance of Khi Solar One with the existing TES system configuration: (a) DNI input, (b) corresponding power output, and (c) amount of thermal power either from solar tower to power generation cycle, from solar tower to TES system, or from TES system to power generation cycle.

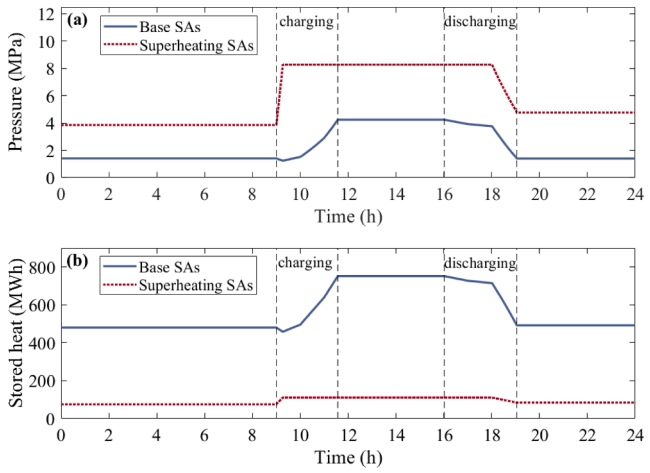

Fig. 11. (a) Pressure, and (b) stored heat in both groups of SAs for the existing TES system. The data presented here is based on operating Khi Solar One under the mean 24-h DNI input profile as of Fig. 10.

process taking place in the evaporator (i.e., States 15 to 16) and the superheater (i.e., States 16 to 3) are indicated by the blue and the red lines, respectively. Once the superheated steam reaches the turbine, it expands to a condensing pressure of 0.018 MPa. Some amount of steam is extracted from the three turbine side extraction points (States 4, 5 and 6) for feedwater heating. The slope of lines representing the expansion processes varies as each line is for different turbine part with different isentropic efficiency as listed in Table 4. The slope of the last expansion process line (i.e., States 6 to 7) is relatively less steep as the last turbine part (i.e., Part 4) has the lowest isentropic efficiency (i.e., 78 %) among other turbine parts. The steam quality at the main turbine outlet is 0.88, still above the minimum boundary for avoiding erosion and corrosion of the steam turbine blades [71].

The dashed lines in Fig. 7 represent the feedwater heating processes in the HP feedwater heater (yellow), in the deaerator (purple), and in the LP feedwater heater (orange). The steam conditions at the hot-side outlet of the HP and the LP feedwater heaters are assumed to be fully saturated liquid. For the HP feedwater heater, the saturated liquid then flows through a steam trap (i.e., throttle) to reduce its pressure in an isenthalpic process from 2.8 MPa to 1.3 MPa (i.e., pressure of the main flow stream flowing into the deaerator) as steam pressure of all deaerator inlets should be the same [72]. Similarly, the pressure of steam flowing from the LP feedwater heater is also reduced by a steam trap from 0.2 MPa to 0.018 MPa (i.e., pressure of the main flow stream flowing into the condenser). The steam is fully condensed in the condenser at 0.018 MPa and then pumped by the condensate pump to 1.34 MPa (i.e., States 9 to 11). After that, the subcooled water is preheated from 58 °C to 117 °C in the LP feedwater heater and then to160 °C in the deaerator. Next, the feedwater is pumped in the feedwater pump to 15.5 MPa before entering the HP feedwater heater. The subcooled water is then heated from 163 °C to 232 °C in the HP feedwater heater with pinch-point temperature differences of 99 °C at the inlet and of 62 °C at the outlet. Finally, the feedwater flows back to the solar tower completing a full cycle. The steam thermodynamic properties for each numbered flow stream are listed in Table C1 of Appendix C.

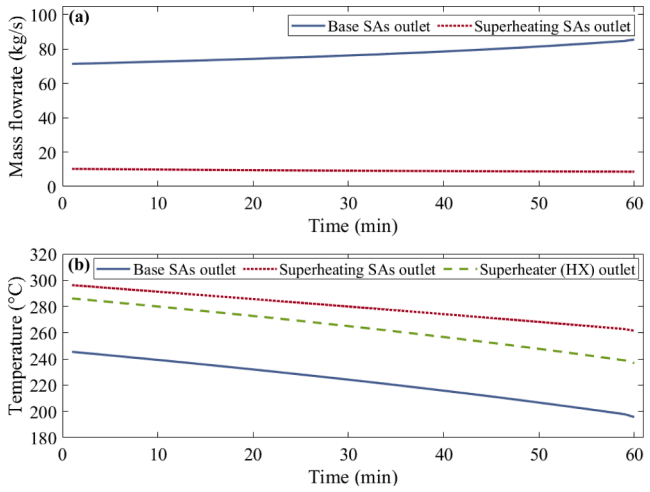

Fig. 12. (a) Mass flowrate, and (b) temperature of steam outflowing from the base and the superheating SAs as well as in the superheating heat exchanger (i.e., turbine inlet) during the main discharging phase (Mode 4) in the existing TES system.

4.2. Performance of Khi Solar One with the existing TES system

4.2.1. Initial base steam accumulators water filling ratio

The analysis of Khi Solar One with the existing TES system starts with determining the initial WFR, defined in Equation (15), of the base SAs. The effect of various base SAs initial WFRs on the final pressure and WFR of the base SAs as well as on the amount of stored heat and discharged electricity from the TES system are shown in Fig. 8. All results were obtained by charging both groups of SAs with saturated steam at 327 °C and 12 MPa. The initial WFR of the superheating SAs for all examined cases is 0.5 as it does not have a significant impact on the overall performance of the TES system. The charging of all SAs stops when either the maximum allowable pressure or the maximum WFR is reached.

In Fig. 8(a), the base SA final pressure reaches the maximum allowable pressure of 4.2 MPa for initial WFRs ranging from 0.3 to 0.75. However, the final WFRs, shown in Fig. 8(b), for the same initial WFR range have not reached the maximum WFR of 0.99. Moreover, the amount of stored heat in the base SA increases from 440 MWh for a WFR of 0.3 to about 860 MWh for a WFR of 0.75. This increase, shown in Fig. 8(c), is due to having more liquid that absorbs the heat from the charging saturated steam. For initial WFRs greater than 0.75, the final pressure of the base SAs is lower than the maximum pressure since the base SAs are already fully filled with steam to their maximum capacity. This can be clearly seen in Fig. 8(b) where the final WFRs have reached to 0.99. Although the base SAs are fully charged with steam, the amount of stored heat decreases when the WFR is higher than 0.75 as the final pressure and temperature of the stored steam is lower for these initial WFRs.

The total discharged electricity from the TES system, presented in Fig. 8(d), has the same behaviour as the amount of the stored heat since more stored heat means higher amount of discharged electricity from the TES system. However, for initial WFRs higher than 0.75, the slope of discharged electricity is much steeper than the slope of the stored heat as not all stored steam is discharged from the same initial pressure (i.e., final pressure after a full charge).

The calculated LCOE and the LCOS of Khi Solar One for the examined range of the base SAs initial WFRs are presented in Fig. 9. The lowest LCOE and LCOS are 256 $/MWh and 225 $/MWh, respectively. Both values are observed when the initial WFR is 0.75. It is expected as the behaviour of the LCOE and the LCOS is inversely related to the total

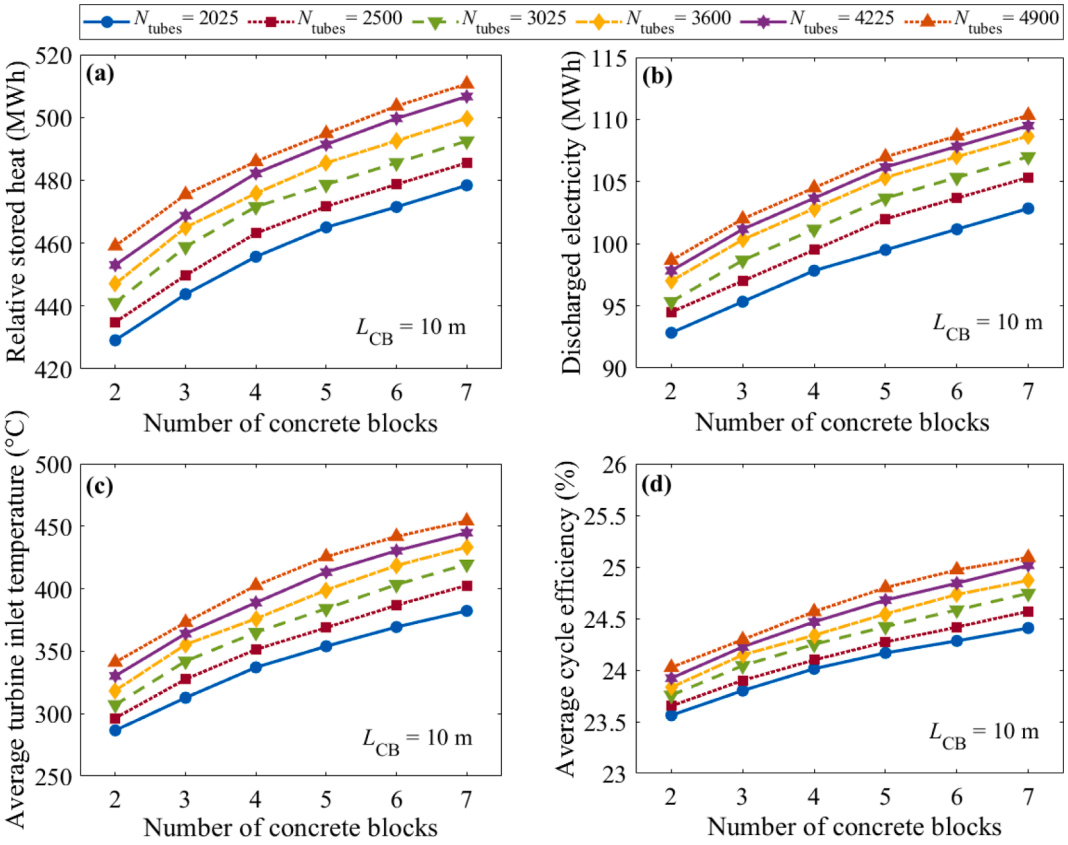

Fig. 13. (a) Stored heat in the TES system, (b) discharged electricity from the TES system, (c) average turbine inlet temperature, and (d) average cycle thermal efficiency during discharging mode operation, for a range of concrete block sizes that have different number of tubes and concrete blocks.

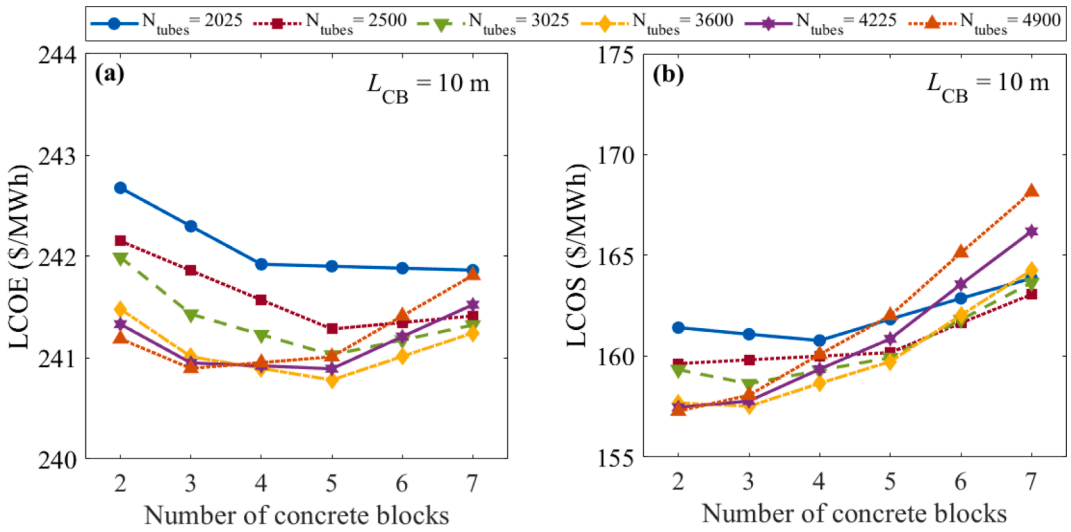

Fig. 14. (a) LCOE, and (b) LCOS for a range of concrete block sizes that have different number of tubes and concrete blocks.

amount of discharged electricity, see Fig. 8(d). Therefore, a WFR of 0.75 for the base SAs is assumed for evaluating the existing TES system as it gives the lowest LCOE and LCOS.

4.2.2. Performance under the mean 24-h DNI profile

The performance of Khi Solar One with the existing TES system under the mean 24-h DNI profile is shown in Fig. 10. The operation of the power plant starts after Hour 7 since the amount of solar irradiance is sufficient to provide heat and to operate the plant at 10 MW of electrical power as shown in Fig. 10(b). The electrical power output increases to 41 MW at Hour 9. During the 2 h period from Hour 8 to Hour 9 (inclusive), the plant is assumed to operate exclusively based on the available solar thermal power in the solar tower (i.e., Mode 1 as discussed in Section 3.5), which is shown in Fig. 10(c) by the darkest shaded area. At Hour 10, the thermal power in the solar tower reaches 214 MW, which is higher than the required amount (150 MW) to generate the 50 MW of electrical power. Therefore, Khi Solar One operates on Mode 2, and the excess thermal power (64 MW) is utilised to evaporate extra steam for storage, i.e., charging phase. The charging phase continues with the increase of the solar power until all SAs are fully charged. The charging phase ends somewhere between Hour 11 and Hour 12 with a total charging time of 152 min. After that, the power plant operates at full rated power until the end of Hour 16.

At Hour 17, though the DNI is only 300 W/m^2, the plant still generates the 50 MW of electrical power. In this case, it extracts some steam from the base SAs for feedwater heating (i.e., Mode 3). The amount of thermal power provided by the TES system for feedwater heating is illustrated by the light blue shaded area in Fig. 10(c). The power plant continues operating on Mode 3 at Hour 18 but at a lower electrical power output of 16.3 MW as there is not enough solar rays at the end of the day. The turbine inlet temperature is constant at 520 °C between Hour 8 and Hour 18 as steam is directly provided by the solar superheater, and the calculated cycle efficiency is 33 %. When the sun is down at the end of Hour 18, the main TES system discharging mode starts (i.e., Mode 4). The stored steam is discharged to operate the power plant at an electrical power of 50 MW for 1 h until the minimum pressure of the base SA is reached. The gradual increase of the TES thermal power during the discharging phase is due to the decrease of pressure and temperature of the discharged steam entering the turbine, which negatively affects the thermal efficiency of the power cycle. Therefore, more heat from the TES system is required to maintain the electrical power level at 50 MW.

The behaviour of the pressure and the amount of stored heat in both groups of SAs are shown in Fig. 11(a) and (b), respectively. The initial amount of stored heat is calculated using ambient temperature and pressure as a reference point. The pressure and the amount of stored heat is constant for both groups of SAs until charging phase is started at the beginning of Hour 10. The superheating SAs are initially charged with saturated steam at a mass flowrate of 50 kg/s until reaching the maximum pressure of 8.2 MPa, taking about 16 min. Simultaneously, some steam is extracted from the base SAs to preheat the extra condensate for storage before entering the solar evaporator. This explains the decrease of pressure and stored heat in the base SAs. After filling the superheating SAs, the charging process of the base SAs starts with a net mass flowrate of 20 kg/s as steam is also extracted from the base SAs for feedwater hating. The pressure of the base group continues increasing at a higher slope (i.e., higher mass flowrate of charging steam) in Hour 11 until the middle of Hour 12 when the charging phase is terminated as the maximum pressure is reached.

The discharging phase precisely starts at the beginning of Hour 17, which can be observed by the decrease of pressure and thermal energy stored in the base SAs as indicated in Fig. 11. However, the discharged steam is only to provide feedwater heating. The main discharging phase (Mode 4) starts at the beginning of Hour 19 and continues for 1 h until terminated when the turbine inlet pressure reached the minimum allowable pressure of 1.4 MPa. The total discharged heat from the TES system is 245 MWh, that is 89 % from the base SAs and 11 % from the superheating SAs. The pressure level of the base group goes back to its initial state. However, the pressure and the stored heat in the superheating group is higher than the initial levels. The remaining extra heat can be discharged the following day. If not, the SAs can be calibrated to its initial state by releasing steam and/or injecting condensate.

The mass flowrate of the steam exiting the base SAs and the superheating SAs during the main discharging phase is shown in Fig. 12(a). At the beginning of the discharge, the steam is released at 71 kg/s. However, the mass flowrate gradually increases to 86 kg/s at the end of the discharge. The increase is to maintain the electrical power level at 50 MW as steam temperature and pressure is decreasing, see Fig. 12(b). Moreover, the mass flowrate of the superheated steam decreases from 10 kg/s at the beginning of the discharge, to 9 kg/s at the end. The decrease is a result of controlling the amount of steam needed to superheat the main flow stream entering the turbine by a maximum of 40 °C. The turbine inlet temperature, i.e., noted as superheater outlet temperature in Fig. 12(b), is 286 °C at the start of the discharge and a calculated cycle efficiency of 25 %. The turbine inlet temperature gradually decreases until it reaches 236 °C (i.e., cycle efficiency is 21 %) due to the reduction of steam pressure and temperature during the discharging phase, which negatively affects the cycle efficiency as well.

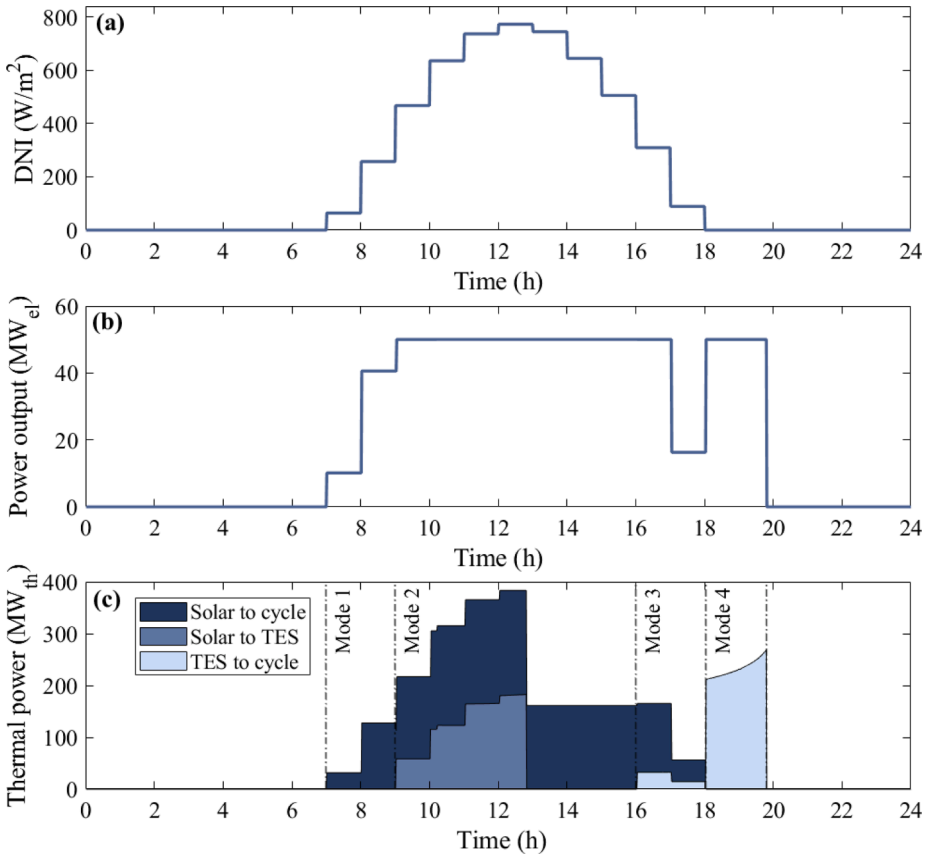

Fig. 15. Diurnal (24-h) performance of Khi Solar One with the extended TES system configuration: (a) DNI input, (b) corresponding power output, and (c) thermal power either from solar tower to power generation cycle, from solar tower to TES system, or from TES system to power generation cycle.

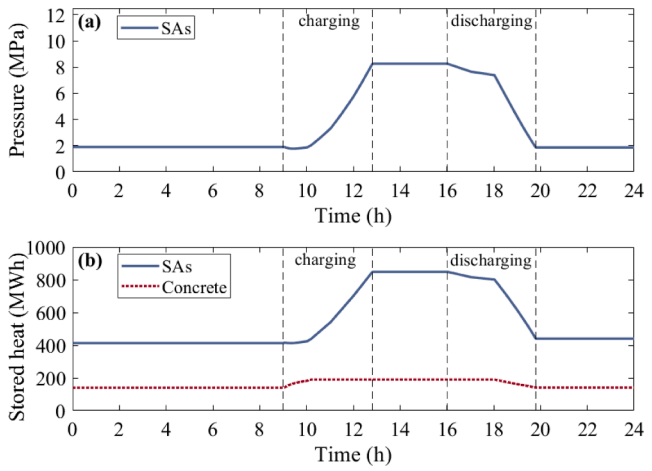

Fig. 16. (a) Pressure, and (b) stored heat in the SAs and in the concrete blocks of the extended TES system. The data presented here corresponds to the same 24-h DNI input profile as of Fig. 15.

4.3. Performance of Khi Solar One with extended TES system configuration

4.3.1. Concrete sizing and thermo-economic parametric study

The analysis of the extended TES system starts by assessing the effect of different concrete sizes on the overall performance of Khi Solar One. The total concrete TES size is determined by the number of tubes distributed inside each block and by the number of concrete blocks with a length (L_{CB}) of 10 m. The tubes are assumed to be equally spaced, horizontally and vertically, in each squared concrete block. The key thermodynamic parameters for a range of concrete TES sizes that have different number of blocks (N_{CB} = 2, 3, 4, 5, 6, and 7), connected in series, and different number of tubes (N_{tubes} = 2025, 2500, 3025, 3600, 4225 and 4900) are compared in Fig. 13. The parametric study was performed using the same SA initial conditions (i.e., initial pressure is 1.9 MPa and initial WFR is 0.5) and the same 24-h DNI profile. Furthermore, the initial temperature profile of the concrete blocks was determined after running the Khi Solar One with the extended TES system model for two charging/discharging cycles (i.e., two days). The charging of concrete blocks is terminated when steam temperature at the last concrete block outlet is higher than 327 °C (i.e., design temperature of SAs). If this temperature is reached and the SAs are not fully charged yet, the charging of SAs is performed directly from the solar evaporator, see Stream 27 in Fig. 2.

Fig. 13(a) shows the relative stored heat in the extended TES system (both SAs and concrete blocks) for the examined range of concrete block sizes. The amount of stored heat in the blocks increases from 427 MWh for the smallest size (N_{tubes} = 2025 and N_{CB} = 2) to 512 MWh for the largest size (N_{tubes} = 4900 and N_{CB} = 7), due to the availability of extra TES media (concrete) in the larger sizes.

The amount of discharged electricity from the TES system for the compared sizes is displayed in Fig. 13(b). The same trend is observed as the amount of discharged electricity depends on the amount of stored heat. Moreover, it can be seen in Fig. 13(c) that the average steam temperature at the turbine inlet increases by 61 %, from 286 °C for the smallest size to 455 °C for the largest size. The increase of temperature is because the larger the concrete blocks size is, the longer the charging time it takes until charging is terminated as more amount of concrete is available. Longer charging time means that concrete reaches higher temperature at the inlet of the first concrete block (i.e., outlet of the last block during discharging mode). Thus, it results in higher steam

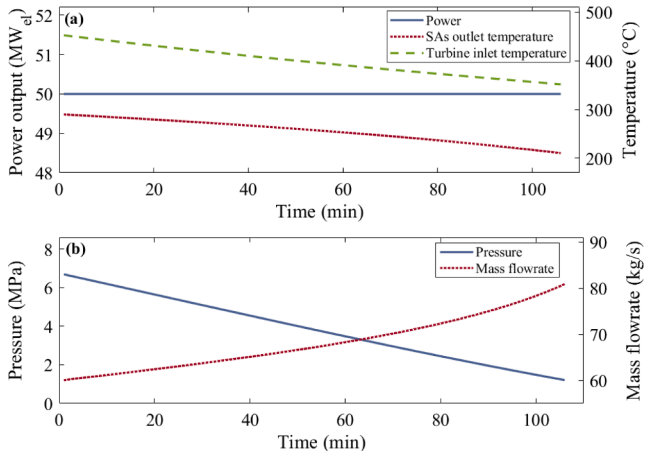

Fig. 17. (a) Khi Solar One power output, on the left *y*-axis, and steam temperature at the SAs outlet and at the turbine inlet, on the right *y*-axis, and (b) turbine inlet pressure, on the left *y*-axis, and steam mass flowrate, on the right *y*-axis, exiting the SAs during the main discharging mode of the extended TES system.

temperature at the concrete block outlet (i.e., turbine inlet) during the discharging phase. Furthermore, the average cycle efficiency during the discharging mode, shown in Fig. 13(d), also increases with larger sizes of concrete blocks. The increase is about 7 %, from 23.6 % for the smallest size to 25 % for the largest sizes and it is a result of the increasing steam temperature at the turbine inlet, which agrees with the definition of Carnot thermal efficiency.

Although the largest concrete TES size provides the highest amount of discharged electricity from the TES system, it might not be the most cost-effective option. Therefore, a comparison of the projected LCOE and LCOS for all examined concrete block sizes are shown in Fig. 14(a) and (b), respectively. The LCOE ranges between 241 $/MWh and 243 $/MWh, with the lowest achieved with 5 concrete blocks, each containing 3600 tubes. The difference of the LCOE between all compared sizes is relatively small as the additional cost of the concrete blocks is insignificant (i.e., $1.2M for the smallest size and $6.9M for the largest size) compared to the total estimated costs of Khi Solar One ($450M). The LCOS ranges from 157 $/MWh to 168 $/MWh. The investment costs of concrete blocks have a greater impact on the LCOS as it can account between 2 % and 12 % of the total capital costs of the extended TES system (i.e., estimated capital costs of SAs is $51.3M).

It is shown in Fig. 14 that the optimal size based on the minimum LCOS is different from the optimal size based on the minimum LCOE. This is because in the LCOE, a major percentage of electricity, above 80 % yearly, is generated without the need of the TES system (i.e., the calculated LCOE without TES system is 268 $/MWh), which results in different behaviour of the LCOE of the power plant. As this study focuses on the performance of Khi Solar One as whole power plant, the concrete TES size with the lowest LCOE ($N_{tubes} = 3600$, $N_{CB} = 5$) is selected for further analyses and for the final thermo-economic comparison with the existing TES system. The dimensions of each selected concrete block are $L_{CB} = 10$ m, $W_{CB} = 4.8$ m, and $H_{CB} = 4.8$ m.

4.3.2. *Performance under the mean 24-h DNI profile*

The performance of the Khi Solar One with the extended TES configuration under the mean 24-h DNI profile is shown in Fig. 15. For the first hours, i.e., from Hour 1 to Hour 9, the operation behaviour of the Khi Solar One with the extended TES system is the same as in the existing configuration as no heat is stored in the TES system. At the beginning of Hour 10, the available thermal power in the solar tower is 212 MW. About 71 % of this power is utilised to generate the 50 MW of electrical power while the remaining 29 % is directed to the TES system. The TES charging process can be split into two modes, and each one takes certain amount of time. The first mode is charging the concrete blocks and the SAs using the superheated steam exiting the solar superheater at 520 °C and 11.5 MPa. The superheated steam deposits some of its heat into the concrete blocks before being accumulated in the SAs. However, this charging mode is only valid when the steam outlet temperature from the last concrete block is

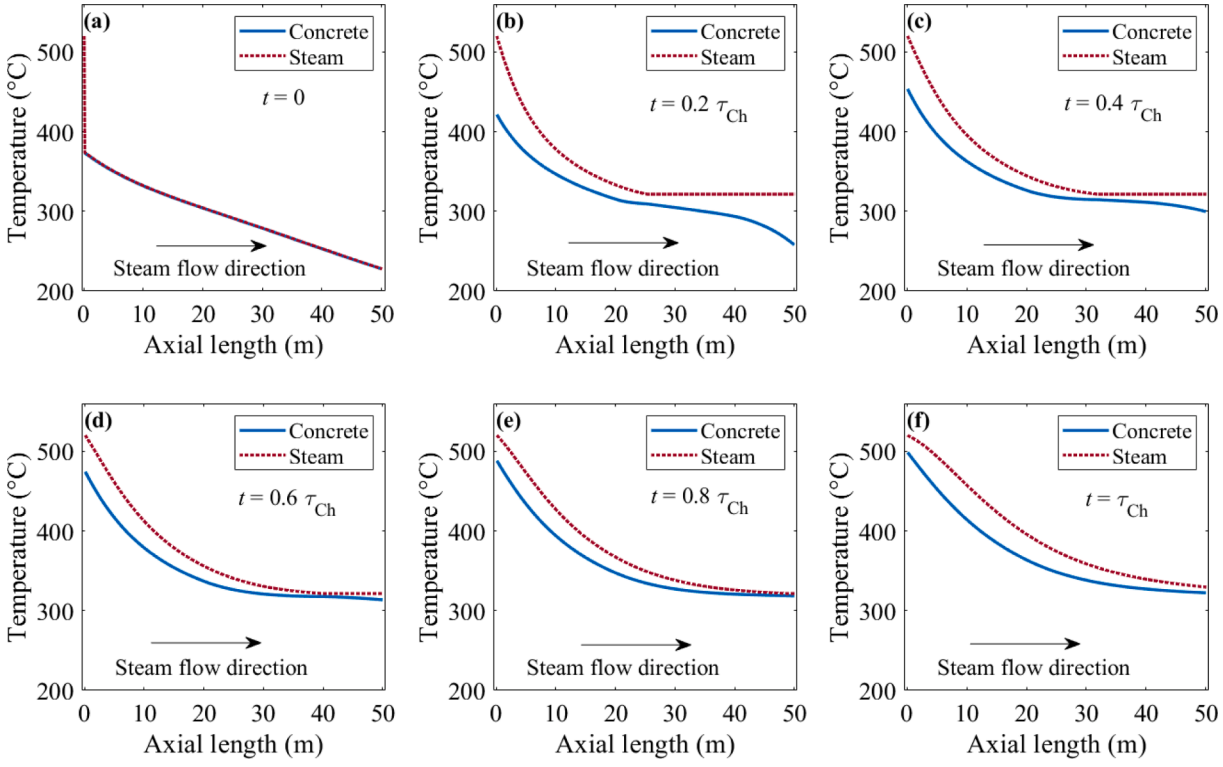

Fig. 18. Progression of concrete and steam temperature profiles during charging mode at different time instants. The total charging time, τ_{Ch}, is 70 min and the steam flow direction is from the left side (from the solar superheater) to the right side (to the SAs).

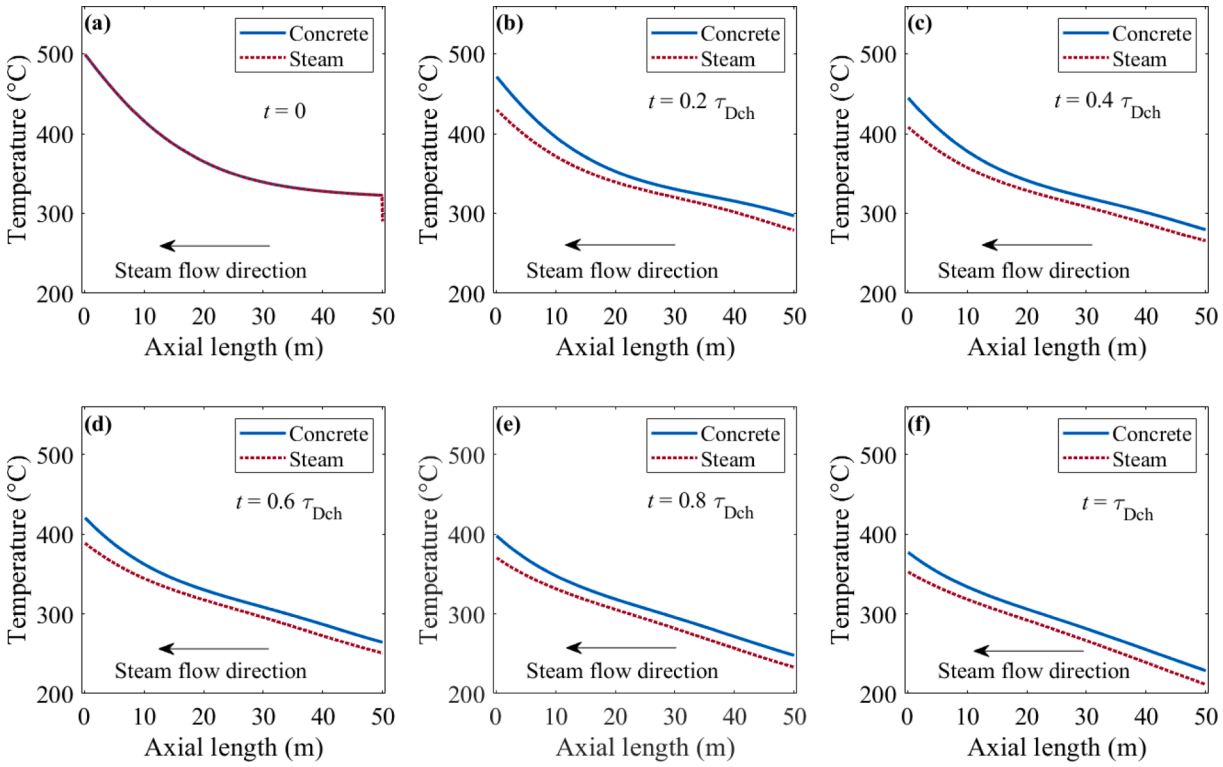

Fig. 19. Concrete and steam temperature profiles during discharging mode at different time instants. The total discharging time, τ_{Dch}, is 106 min and the steam flow direction is from the right side (from the SAs) to the left side (to the steam turbine).

327 °C or less. When the steam temperature is above this point, the second charging mode starts, which is charging the SAs directly from the solar evaporator and bypassing the concrete blocks. The charging of SAs continues until reaching a maximum pressure of 8.2 MPa. The calculated total charging time is 227 min, that is 70 min for the first mode and 157 min for the second mode. It is about 45 % longer than the total charging time in the existing TES system due to the additional storage capacity provided by concrete and also to the ability to charge the SAs to a higher pressure compared to the base SAs in the existing TES system. There is a slight step increase in the total thermal power after Hour 10, see Fig. 15(c), which occurs after changing from the first to the second charging mode. This increase is because the solar evaporator has a higher efficiency than the superheater, thus, higher amount of thermal power is available in the evaporators for the same amount of CSP.

After the full charge of the TES system that occurs before the end of Hour 13, Khi Solar One continues operating at 50 MW of electrical power until the end of Hour 17. During Hour 17, the plant operates on Mode 3 (i.e., defined in Section 3.5) where feedwater heating is supplied by the SAs as indicated in the lightest blue shaded area in Fig. 15(c). At Hour 18, Khi Solar One continues operating on Mode 3 but at 16.3 MW of electrical power as the available thermal power in the solar tower is not sufficient for maximum power output. Like in the existing configuration, the turbine inlet temperature is 520 °C and the cycle efficiency is 33 % between Hour 8 and Hour 18 as steam is directly provided by the solar superheater. The main discharging phase (Mode 4) starts at the beginning of Hour 19 and continues until the turbine inlet pressure reaches the lowest allowable pressure of 1.4 MPa (i.e., SAs pressure is 1.9 MPa considering a 0.5 MPa pressure drop in the concrete blocks). The total discharging time is 106 min and the total generated electricity utilising the stored heat is 88 MWh. The non-linear increase of TES system thermal power during the discharging phase, shown in Fig. 15(c), is needed to maintain the electrical power output at 50 MW. The need of extra power is due to continuous decrease of the discharging cycle efficiency caused by the reduction of steam temperature and pressure at the turbine inlet while steam is discharged from the SAs.

The behaviours of the SAs pressure and the amount of stored heat in TES system for the same 24-h DNI profile are shown in Fig. 16(a) and (b), respectively. The amount of stored heat was calculated by taking ambient condition as a reference point. The SA pressure is constant at 1.9 MPa until the beginning of Hour 10. During this hour, although SAs are charged with steam, the pressure is slightly decreasing. This is because some amount of steam is simultaneously discharged from the SAs to preheat the condensate that is allocated for storage in the HP feedwater heater, i.e., flow stream number 17 in Fig. 2. However, the total amount of thermal energy stored in the SAs during the same hour is still increasing because of two main reasons: (i) the SAs are charged with steam at a higher mass flowrate (35 kg/s) than the mass flowrate of discharged steam (26 kg/s) for condensate preheating; and (ii) the temperature of the charging steam increases from 262 °C at the beginning of the charge to 321 °C at the end as a result of the decreasing heat transfer rate between the steam and the concrete. This can be seen by the gradually decreasing slope of the amount of stored heat in the concrete. The reduction of the heat transfer rate is mainly due to the increasing temperature of the concrete while charging, which decreases the temperature difference between the two media, thus, reducing the heat transfer rate.

As the available thermal power for storage increases at the beginning of Hour 11, the steam mass flowrate existing the superheater increases from 35 kg/s to 66 kg/s. The charging continues in the concrete for the first 10 min in Hour 11 but then stops as the steam temperature reaches 327 °C at the last concrete block outlet. It can be seen in Fig. 16(b) that the rate of heat transfer (i.e., the slope of stored heat) during these10 min is higher than the heat transfer rate at the end of Hour 10. This is due to the increase of the steam mass flowrate, which increase the effective heat transfer coefficient and thus the rate of heat transfer from steam to concrete. The SAs are not fully charged at this point, therefore, the charging of SAs continues by diverting steam directly from the solar evaporator until reaching the maximum pressure of 8.2 MPa. At the end of the charging phase, the total stored heat in the extended TES system is 1040 MWh, that is 850 MWh in the SAs and 190 MWh in the concrete blocks.

The discharging phase technically starts at Hour 17 when steam is discharged for feedwater heating as in the existing TES system.

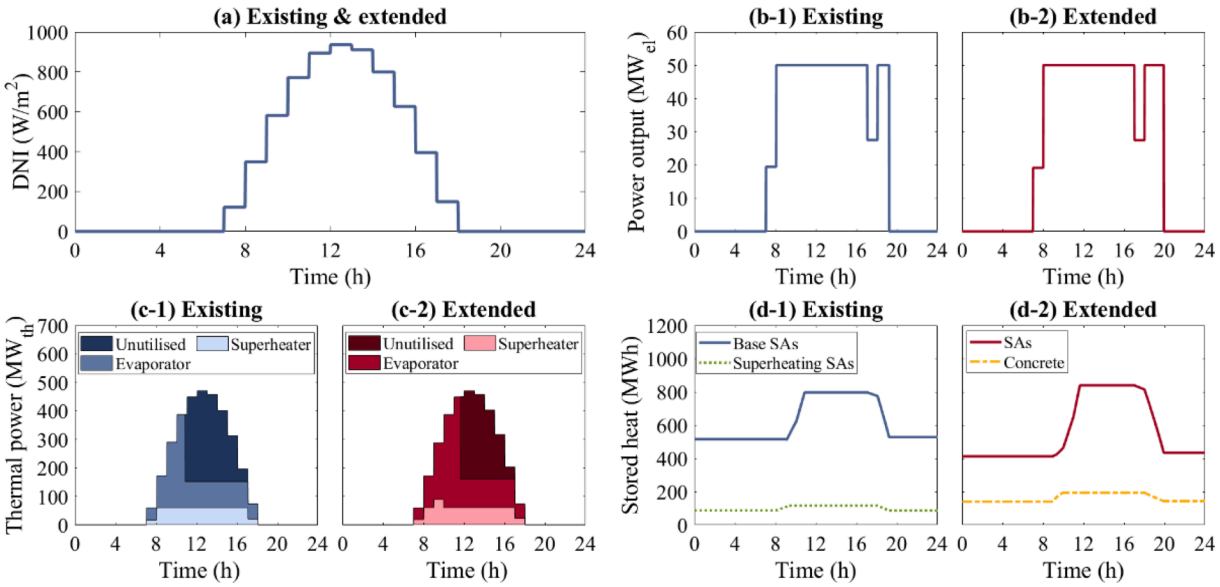

Fig. 20. Comparison of the thermodynamic performance of the existing and the extended TES systems for DNI Profile 1 as defined in Section 3.5, for: (b-1, c-1, d-1) existing TES system, and (b-2, c-2, d-2) extended TES system.

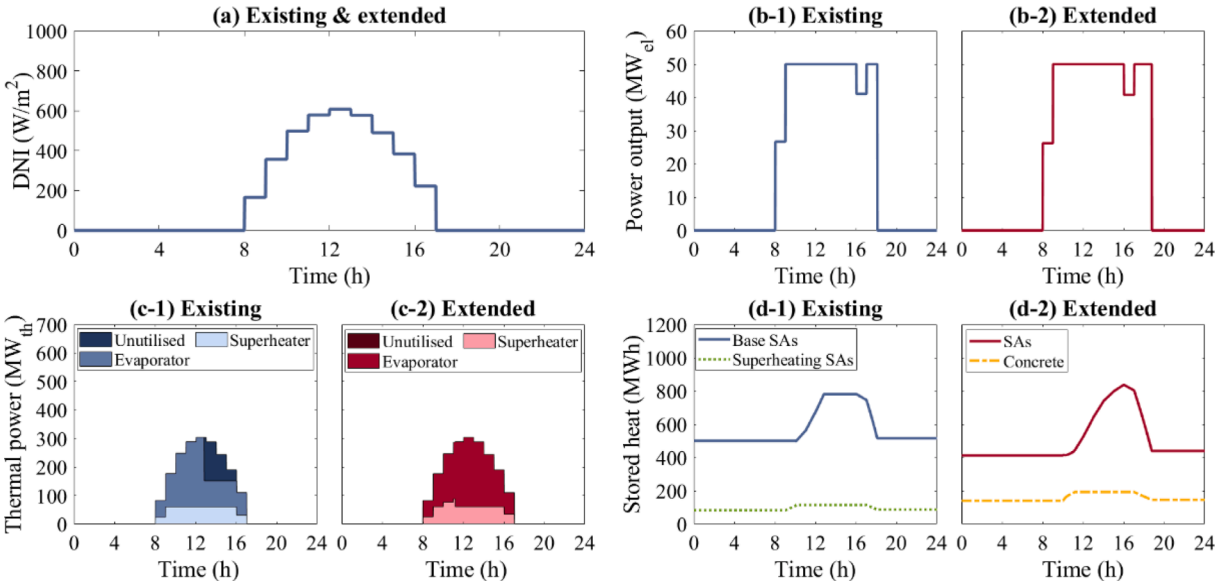

Fig. 21. Comparison of the thermodynamic performance of the existing and the extended TES systems for DNI Profile 2 as defined in Section 3.5, for: (b-1, c-1, d-1) existing TES system, and (b-2, c-2, d-2) extended TES system.

Table 12
Estimated capital costs of SAs and storage heat exchanger.

Method	SAs ($M)	Heat exchanger ($k)
Seider et al. [57]	41.6	360
Turton et al. [59]	–	320
Couper et al. [60]	53.0	130
Ulrich et al. [61]	59.3	110
Average capital costs	**51.3**	**230**

Table 13
Estimated capital costs of the 5 concrete blocks with $N_{tubes} = 3600$ and $L_{CB} = 10$ m.

Components	Cost ($k)
Concrete mixture	340
Tubes	130
Insulation	370
Foundation	680
Platform and steel	630
Interconnecting piping and valves	210
Electrical	210
Instrumentation and control	210
Contingency	420
Engineering	420
Construction	560
Total costs	**4180**

However, the main discharging phase (Mode 4) starts at Hour 19 and continues for 107 min until the SA pressure is 1.9 MPa. The total discharged heat is 460 MWh, that is 410 MWh from the SAs and 50 MWh from the concrete blocks. The heat addition in the concrete is entirely utilised to superheat the saturated steam released from the SAs before entering the steam turbine. Although the SAs pressure at the end of the

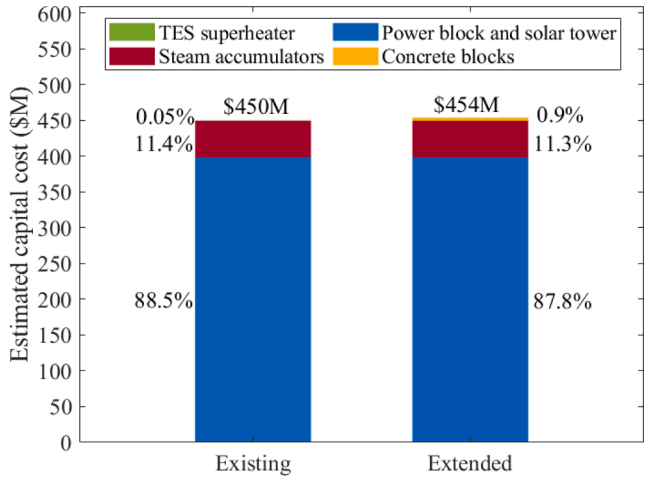

Fig. 22. Estimated total capital costs of the main components of Khi Solar One with the two analysed TES system configurations (existing and extended).

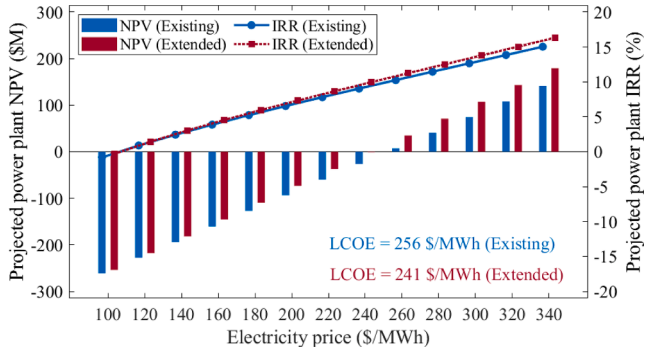

Fig. 23. Comparison of the projected NPV and the projected IRR of Khi Solar One with the two TES system configurations (existing and extended) for electricity prices from 100 $/MWh to 340 $/MWh.

discharge is the same as at the beginning of the day, the amount of the heat is still higher as the post discharge WFR of the SAs is 0.53, which is higher than the initial WFR (0.5). Such difference is a result of the time varying charging temperatures and discharging rates. However, the final WFR can be calibrated to its initial state by releasing steam and/or injecting condensate.

Fig. 17 shows the main steam parameters during the discharging phase of the extended TES system. The steam temperature at the SAs outlet is gradually decreasing from 289 °C (i.e., the saturation temperature of steam at 7.4 MPa) at the start of the main discharging phase to 210 °C (i.e., the saturation temperature of steam at 1.9 MPa) at the end. However, the discharged steam temperature is increased by an average of 154 °C due to heat by the concrete blocks. The turbine inlet temperature at the start of the main discharging phase is 452 °C, which is 58 % higher than the maximum inlet temperature (268 °C) in the existing TES system configuration. The calculated cycle efficiency at this point is 29 %, that is 16 % improvement of the highest discharging cycle efficiency (25 %) calculated in the existing TES system. The turbine inlet temperature gradually decreases as the pressure and the temperature of steam exiting the SAs and then the concrete blocks decrease during the discharge, which negatively affects the cycle efficiency. The lowest turbine inlet temperature that occurs at the end of the discharging phase is 352 °C with a cycle efficiency of 22 %. These two values are still respectively 50 % and 5 % higher than those calculated in the existing TES system. The pressure shown on the left *y*-axis of Fig. 17(b) is the turbine inlet pressure, which is 0.5 MPa lower than the pressure of discharged steam from the SAs to account for the assumed pressure drop. To maintain the electrical power output at 50 MW with the decreasing steam pressure and temperature, the steam mass flowrate is gradually increased as shown on the right *y*-axis of Fig. 17(b).

4.3.3. *Temperature profiles of concrete during charging/discharging processes*

The temperature progression of the concrete and the steam (in all 5 concrete blocks with a total length $L_{total} = 50$ m) during the charging phase is shown in Fig. 18. The steam flow direction is from the left (i.e., from the solar superheater) to the right (i.e., to the SAs). Fig. 18(a) shows the temperature profile at time zero, just before the start of the charging mode. The initial concrete temperature profile was obtained after running the formulated TES system model for two charging/discharging cycles using the mean 24-h DNI profile. The steam temperature inside the tubes is initially assumed to be the same temperature as of the concrete, and the inlet steam temperature (i.e., boundary condition) is 520 °C.

After a time of 0.2 τ_{Ch} (14 min), the concrete temperature at the inlet has already increased to 412 °C as shown in Fig. 18(b). At the same time instant, the temperature of steam decreases along the axial length of the concrete blocks until reaching the saturation temperature of 321 °C at 11.5 MPa. At this point, the latent heat of steam is being transferred to the concrete elements. The boundary of the single-phase and the two-phase regions shifts from the left to the right, shown in Fig. 18(c), (d) and (e) as charging continues and the concrete temperature is increasing. The temperature difference between the steam in the two-phase region and the concrete decreases as more heat is transferred from the steam to the concrete. The charging phase stops at τ_{Ch} when the steam temperature is 327 °C at the outlet. At this time, the highest concrete temperature is 489 °C (at the inlet of the first concrete block) and the lowest is 322 °C (at the outlet of the last concrete block) as

Table 14
Main thermodynamic and economic results of Khi Solar One with the existing and the extended TES system configurations. The results were obtained using the mean 24-h DNI profile for the entire year, an electricity price of 280 $/MWh, and the extended TES system has five concrete blocks with $N_{tubes} = 3600$, $L_{CB} = 10$ m, $W_{CB} = 4.8$ m, and $H_{CB} = 4.8$ m.

Parameter	Existing	Extended	Difference (%)
Generated electricity from Khi Solar One (MWh/day)	517	556	7.5
Generated electricity from the TES system (MWh/day)	67	106	58
Full TES discharge duration (min)	60	107	78
Maximum cycle thermal efficiency at discharging phase (%)	25	29	16
Average cycle thermal efficiency at discharging phase (%)	23	26	13
Maximum turbine inlet temperature at discharge (°C)	286	453	58
Average turbine inlet temperature at discharge (°C)	263	400	52
Total power plant capital cost ($M)	450	454	0.9
LCOE ($/MWh)	256	241	−5.9
LCOS ($/MWh)	225	159	−29
Payback time (years)	18.3	15.6	−15
NPV ($M)	41	71	73
IRR (%)	11.5	12.5	8.7

shown in Fig. 18(f).

The steam and the concrete temperature profiles during the discharging phase are shown in Fig. 19. The total discharging time (τ_{Dch}) is 106 min and the steam flow direction is from the left (from the SA) to the right (to the turbine). At time zero and before the discharging phase, the steam temperature is assumed to be the same as the concrete temperature, see Fig. 19(a), since steam has been held inside the tubes for hours after the charging phase. The steam temperature at the first concrete block entrance from the SAs side (i.e., left boundary condition) is 289 °C, which is the temperature of the steam exiting the SAs. During the discharging phase, the concrete and the steam temperature profiles decreases as shown in Fig. 19(b) to (f). Moreover, the inlet steam temperature (i.e., on the left side) is also decreasing with time as the pressure and the temperature of all SAs are decreasing during the discharging phase.

4.4. Thermo-economic comparison of existing vs. extended TES configurations

4.4.1. Evaluation at different 24-h DNI profiles

The performance of Khi Solar One with the existing and the extended TES for the proposed DNI profiles (i.e., defined in Section 3.5) are shown in Figs. 20 and 21. In both figures, (a) shows the DNI input profile, (b) shows the output power, (c) shows the available thermal power, and (d) shows the amount of stored heat in the TES system. For example, Fig. 20 shows the performance of Khi Solar One using DNI Profile 1, which is the mean plus one standard deviation of the collected DNI data. During the main TES discharging mode that starts at Hour 18, the amount of electricity generated utilising the stored heat in the extended TES system is 97 MWh while it is only 57 MWh for the existing TES system, a relative increase of 70 %. It is also shown in Fig. 20(c) that the extended TES configuration is able to utilise about 60 %, that is 2 GWh, of the available heat in the solar receivers (3.36 GWh), whereas only about 46 % (1.54 GWh) is employed in the existing TES system. This is mainly due to the ability of the extended TES system configuration to utilise the maximum storage capacity of the existing SAs at maximum pressure, as well as to the addition of the concrete blocks.

Fig. 21 compares the performance of Khi Solar One with the two TES system configurations at DNI Profile 2, which is the mean minus one standard deviation of the DNI data. In this DNI profile, the availability of sufficient sunlight is only for 9 h (from Hour 9 to Hour 17), whereas in the mean DNI is 11 h (from Hour 8 to Hour 18). The estimated total heat in the solar receivers is 1.9 MWh. As shown in Fig. 21(c), all this heat is utilised for electricity generation in the extended TES system while only 85 % of heat is utilised in the existing TES system.

4.4.2. Cost and economic performance of both configurations

The estimated capital costs of the SAs and of the storage heat exchanger in the existing TES system are listed in Table 12. The considered costs in this paper are the average value of the obtained costs from the four different methods, which are discussed in Section 3.4.1. The total capital cost of the existing TES system is about $51.5M, that is $51.3M for the SAs, and $230k for the storage heat exchanger. The Turton et al. [59] method predicts SA costs at least eight times higher than other methods (i.e., $445M). Thus, it is excluded from this study. The maximum and the minimum SA costs are within ± 20 % of the average cost, which is acceptable when it comes to cost estimation uncertainties. For the heat exchanger costs, the effect of cost variations is minor as it only accounts for 0.2–0.7 % of the total capital costs of the exiting TES system. Therefore, taking the maximum, the minimum, or the average estimated cost for heat exchanger units does not have a significant effect on the thermo-economic study.

The estimated costs of the materials and the construction of the 5 concrete blocks ($N_{tubes} = 3600$, $L_{CB} = 10$ m, and $W_{CB} = H_{CB} = 4.8$ m) in the extended TES system are summarised in Table 13. The total cost is $4.2M, that is $2.8M for the materials (i.e., direct) and $1.4M for indirect costs.

The estimated capital costs of Khi Solar One with the two TES system configurations are compared in Fig. 22. The total costs of Khi Solar One with the existing TES system is $450M (11 % of this is for the TES system), while is about $454M with the extended TES system (12 % of this is for the TES system). The cost difference between the two TES configurations is $4M, less that the total estimated cost of concrete ($4.2M), since the $230k storage superheater is no longer needed in the extended configuration.

The economic performance of Khi Solar One with the existing and the extended TES configurations are presented in Fig. 23. The left *y*-axis of Fig. 23 compares the projected NPV of Khi Solar One for a range electricity prices, from 100 $/MWh to 340 $/MWh, and the right *y*-axis compares the projected IRR for the same price range. Installation of 5 concrete blocks, connected in series, with $N_{tubes} = 3600$ and $L_{CB} = 10$ m is assumed in the extended configuration as they offer the lowest LCOE among the examined size range. The projected NPV of both TES system configurations are negative for electricity prices ranging from 100 $/MWh to 240 $/MWh. In particular, the NPV for the extended case is almost zero at an electricity price of 240 $/MWh. Khi Solar One could generate positive returns if it operates in electricity markets with prices higher than 260 $/MWh. In the examined range of electricity prices, the projected NPV of the extended TES system configuration is always higher than the existing TES system configuration. This is due to the ability of storing greater amount of heat, about 177 MWh of extra heat, with an additional investment of $4.2M. The addition of concrete blocks allows for extra TES capacity and for storing steam at higher pressure limits in the SAs. The difference between the two NPVs increases with the increasing electricity prices as more income could be generated from selling the extra electricity produced in the extended TES system (i.e., 39 MWh/day). Since the discount rate is 10 %, the NPVs are negative for electricity prices that have IRRs lower than 10 % and are positive for IRRs higher than 10 %.

The breakeven point where the NPV is zero and the IRR is 10 % is at an electricity price of 256 $/MWh for the existing TES system and of 241 $/MWh for the extended TES system. Thus, based on the analyses and assumptions made in this study, the existing TES configuration could provide positive returns if the generated electricity is sold at a price higher than 256 $/MWh and the extended TES configuration could be economically positive if the generated electricity is sold at a price higher than 241 $/MWh. The breakeven prices are equal to the calculated LCOE of both TES systems, reported in Fig. 23.

The key thermodynamic and economic results of Khi Solar One with the existing and the extended TES system configurations are compared in Table 14. The results were obtained using the mean 24-h DNI profile for the whole year and an electricity price of 280 $/MWh. Taking the existing configuration as a reference, the extended TES system configuration is able to deliver 58 % more electricity than the existing TES system, that is 7.5 % extra if considering the power output of Khi Solar One. Moreover, the extended configuration can store heat at a higher temperature than the existing configuration, which increases the average turbine inlet temperature by 52 % (i.e., 263 °C for existing and 400 °C for extended) during the TES discharging mode. The temperature increase enhances the maximum and the average cycle thermal efficiency during the discharging mode by 16 % and 13 %, respectively.

The improved thermodynamic performance of the extended TES configuration could be achieved with an estimated additional capital cost of $4.2M, i.e., the cost of the concrete blocks. With this additional cost, the calculated LCOS and the LCOE are respectively 29 % and 6 % lower than those with the existing configuration. At an electricity price of 280 $/MWh, Khi Solar One with the extended configuration could achieve a NPV of $71M whereas it is only $41M for the existing configuration, which is about $30M extra in total revenues for the 25 years (i.e., lifetime of the power plant). The payback time, which is defined as the number of years required until achieving a zero NPV, of

Khi Solar One with the extended TES system is 2.7 years shorter than with the existing TES system.

5. Conclusions

Two steam accumulating thermal energy storage (TES) options for direct steam generation (DSG) concentrated solar power (CSP) plants were compared taking the Khi Solar One power plant in South Africa as a case study. The compared TES options were: (i) the existing TES system in Khi Solar One, which consists of two groups of steam accumulators (SAs) and a superheater; and (ii) an extended TES system that contains one group of SAs and concrete blocks for higher-temperature storage. The two configurations were thermodynamically and economically analysed using the same existing solar tower and the same power generation cycle components in Khi Solar One.

The thermodynamic analysis of the existing TES system started by determining the initial water filling ratio (WFR) of the base SAs that maximises profitability. It was found that base SAs with initial WFRs of 0.75 gives the lowest levelised cost of electricity (LCOE) of 256 $/MWh. Moreover, different number of concrete blocks with various sizes, in terms of number of tubes, were thermodynamically investigated using a transient heat and mass energy balance computational model, and also economically compared applying the same economic assumptions. It was found that installing five 10-m long concrete blocks, connected in series, with 3600 equally-spaced tubes offers the lowest LCOE of 241 $/MWh.

The performance of Khi Solar One with the existing and with the extended TES systems were compared for the same 24-h hourly direct normal irradiance input, and the following remarks can be given:

- The extended configuration can store an extra 177 MWh of heat using the same number of SAs as in the existing configuration and the additional concrete blocks. The TES capacity increase is mainly due to the ability of the extended configuration to utilise the current SAs to store steam at a higher temperature and pressure, as superheating is achieved by the higher-temperature concrete TES unit.
- Maximising the use of the current SAs and the addition of concrete blocks result in an averaged additional electricity of 39 MWh per day.
- During TES system discharging mode, the average cycle thermal efficiency is 13 % higher in the extended configuration as the inlet temperature can reach up to 453 °C while the maximum is 286 °C in the existing TES system configuration.
- With an estimated additional investment cost of $4.2M (i.e., cost of concrete blocks) that only accounts for 1 % of the total cost of Khi Solar One, the extended TES system configuration could decrease the LCOE of the DSG CSP plant by 6 %, from 256 $/MWh to 241 $/MWh.
- Extending the existing TES configuration increases the projected net present value of Khi Solar One from $41M to $71M if the generated electricity is sold at 280 $/MWh.

The key results of the present work show that combining concrete blocks with SAs as TES option have greater economic potential than using SAs only. However, the study was limited to considering thermodynamic and economic sensitivity analysis of semi-defined concrete block and tube dimensions with no size optimisation and with a reduced-order concrete TES model. Therefore, future work related to this study will include: (i) concrete block size optimisation in terms of concrete block dimensions, tube diameter and thickness, and diameter of the surrounded concrete mixture; (ii) thermodynamic performance evaluation of the transient operation of the DSG CSP plant with the two TES options for the entire year instead of selected days only; (iii) formulation and analysis of a transient 3-D computational model for the concrete blocks for more accurate results; and (iv) economic evaluation of constructing similar size DSG CSP plants in other geographical locations or countries that have different electricity market structures.

CRediT authorship contribution statement

Abdullah A. Al Kindi: Conceptualization, Data curation, Formal analysis, Methodology, Software, Validation, Visualization, Writing – original draft, Writing – review & editing. **Paul Sapin:** Formal analysis, Methodology, Software, Writing – review & editing. **Antonio M. Pantaleo:** Conceptualization, Formal analysis, Writing – review & editing. **Kai Wang:** Formal analysis, Methodology, Software, Writing – review & editing. **Christos N. Markides:** Conceptualization, Formal analysis, Funding acquisition, Methodology, Project administration, Resources, Supervision, Writing – review & editing.

Declaration of Competing Interest

The authors declare that they have no known competing financial interests or personal relationships that could have appeared to influence the work reported in this paper.

Data availability

Data will be made available on request.

Acknowledgment

This work was supported by the UK Engineering and Physical Sciences Research Council (EPSRC) [grant numbers EP/R045518/1, and EP/S032622/1]. The work was also supported by the UK Department of International Development (DFID) through the Royal Society-DFID Africa Capacity Building Initiative and by the Government of the Sultanate of Oman. Data supporting this publication can be obtained on request from cep-lab@imperial.ac.uk. For the purpose of Open Access, the authors have applied a CC BY public copyright licence to any Author Accepted Manuscript version arising from this submission.

Appendix A. – Details and validation of steam accumulator model

Predictions of the mass, pressure and energy of the steam/water in the SA were performed using mass conservation and the energy balance equations of the thermal equilibrium model developed by Stevanovic et al. [44]. The rates of change of the water (liquid) and steam (vapour) mass in the SA were calculated using:

$$\frac{dm}{dt} = \Delta\dot{m}_V + \Delta\dot{m}_L \tag{A.1}$$

$$\Delta\dot{m}_V = \dot{m}_{V,in} - \dot{m}_{V,out} \tag{A.2}$$

$$\Delta\dot{m}_L = \dot{m}_{L,in} - \dot{m}_{L,out} \tag{A.3}$$

The SA enthalpy variations were predicted using:

$$\frac{dH}{dt} = \Delta(\dot{m}h)_V + \Delta(\dot{m}h)_L + V\frac{dP}{dt} \tag{A.4}$$

$$\Delta(\dot{m}h)_V = (\dot{m}h)_{V,in} - (\dot{m}h)_{V,out} \tag{A.5}$$

$$\Delta(\dot{m}h)_L = (\dot{m}h)_{L,in} - (\dot{m}h)_{L,out} \tag{A.6}$$

To calculate the transient pressure and mass of steam in the SAs during charging and discharging, the following steps and equations were used:

1 The total enthalpy of the SA is:

$$H = mh \tag{A.7}$$

2 Differentiating with respect of time:

$$\frac{dH}{dt} = h\frac{dm}{dt} + m\frac{dh}{dt} \tag{A.8}$$

3 The specific enthalpy can be calculated by:

$$h = h' + x\Delta h_{vap} \tag{A.9}$$

where superscript ‘’’ stands for saturated liquid conditions.

4 Taking the derivative of the specific enthalpy:

$$\frac{dh}{dt} = \frac{dh'}{dt} + \Delta h_{vap}\frac{dx}{dt} + x\frac{d\Delta h_{vap}}{dt} \tag{A.10}$$

5 Rearranging and introducing rate of change of pressure dP/dt:

$$\frac{dh}{dt} = \left(\frac{dh'}{dP} + x\frac{d\Delta h_{vap}}{dP}\right)\frac{dP}{dt} + \Delta h_{vap}\frac{dx}{dt} \tag{A.11}$$

6 The steam quality, x, can be predicted by:

$$x = \frac{\nu - \nu'}{\nu'' - \nu'} \text{ where } \nu = \frac{V}{m} \tag{A.12}$$

7 Taking the derivative of steam quality, x, and specific volume, ν, with respect of time or pressure, and knowing that SA volume, V, is constant:

$$\frac{dx}{dt} = -\frac{1}{m}\frac{\nu}{\nu'' - \nu}\frac{dm}{dt} - \left(\frac{1}{\nu'' - \nu'}\frac{d\nu'}{dP} + \frac{\nu - \nu'}{(\nu'' - \nu')^2}\frac{d(\nu'' - \nu')}{dP}\right)\frac{dP}{dt} \tag{A.13}$$

8 Finally, the rate of change of SA pressure can be calculated by substituting Equations (A.7)-(A.13) into Equation (A.4) and rearranging:

$$\frac{dP}{dt} = \frac{\Delta(\dot{m}h)_V + \Delta(\dot{m}h)_L + \left(\frac{\Delta h_{vap}\frac{V}{m}}{\nu'' - \nu'} - h\right)(\Delta\dot{m}_V + \Delta\dot{m}_L)}{m\left(\frac{dh'}{dP} + \frac{\frac{V}{m} - \nu'}{\nu'' - \nu'}\frac{d\Delta h_{vap}}{dP} - \frac{\Delta h_{vap}}{\nu'' - \nu'} - \frac{d\nu'}{dP} - \Delta h_{vap}\frac{\frac{V}{m} - \nu'}{(\nu'' - \nu')^2}\frac{d(\nu'' - \nu')}{dP}\right) - V} \tag{A.14}$$

Table A1
Initial conditions and main SA parameters for SA model validation.

Parameter	Test A	Test B	Test C
SA volume (m^3)	64	64	64
SA initial pressure (MPa)	3.4	2.5	5.0
SA initial WFR (-)	0.5	0.5	0.5
Charging/discharging mode	charging	charging	discharging

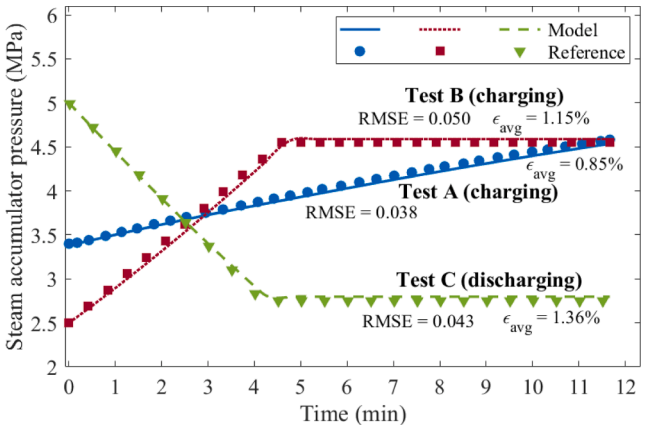

Fig. A1. Comparison of the behaviour of the SA pressure between the model and Ref. [44] results for all tests. Tests A and B indicate the increase of SA pressure during steam charging while Test C shows the decrease of SA pressure during the discharge.

Validation of the formulated SA model was conducted using the set of data for three different SA charging and discharging tests (i.e., Tests A, B and C) reported in Ref. [44]. The same initial conditions and charging/discharging steam parameters, as listed in Table A1 and reported in detail in Refs. [44,73], were used to validate the formulated model.

The calculated/predicted and reference SA pressures for all tests are compared in Fig. A1. The comparison shows that the formulated model is sufficiently accurate as the maximum RMSE is 0.05 and the maximum average relative error (ϵ_{avg}) is 1.4 %. The small source of error could be a result of adopting a different way of calculating the rate of change of steam properties at different pressure points. Stevanovic et al. [44] state that their equilibrium model can have a 6 % estimation error when compared to a non-equilibrium model also proposed in Ref. [44], but both have the same initial and final pressure points. However, the non-equilibrium model requires inner physical parameters and dimensions of the SA which is not available in the present study. Therefore, the equilibrium model has been used here.

Appendix B. – Validation of concrete thermal energy storage model

The formulated concrete storage model was validated using experimental data from Ref. [49]. Two experimental data sets that differ in terms of the HTF volumetric flowrate and initial temperature profile in the concrete were examined. Fig. B1 compares the model predictions with the experimental data reported in Ref. [49]. The HTF and solid temperatures for a HTF volumetric flowrate of 3 m^3/h are shown in Fig. B1(a) and (b), while for a HTF volumetric flowrate of 4.5 m^3/h the same quantities are shown in Fig. B1(c) and (d), respectively. All experimental data are plotted using dots, while the

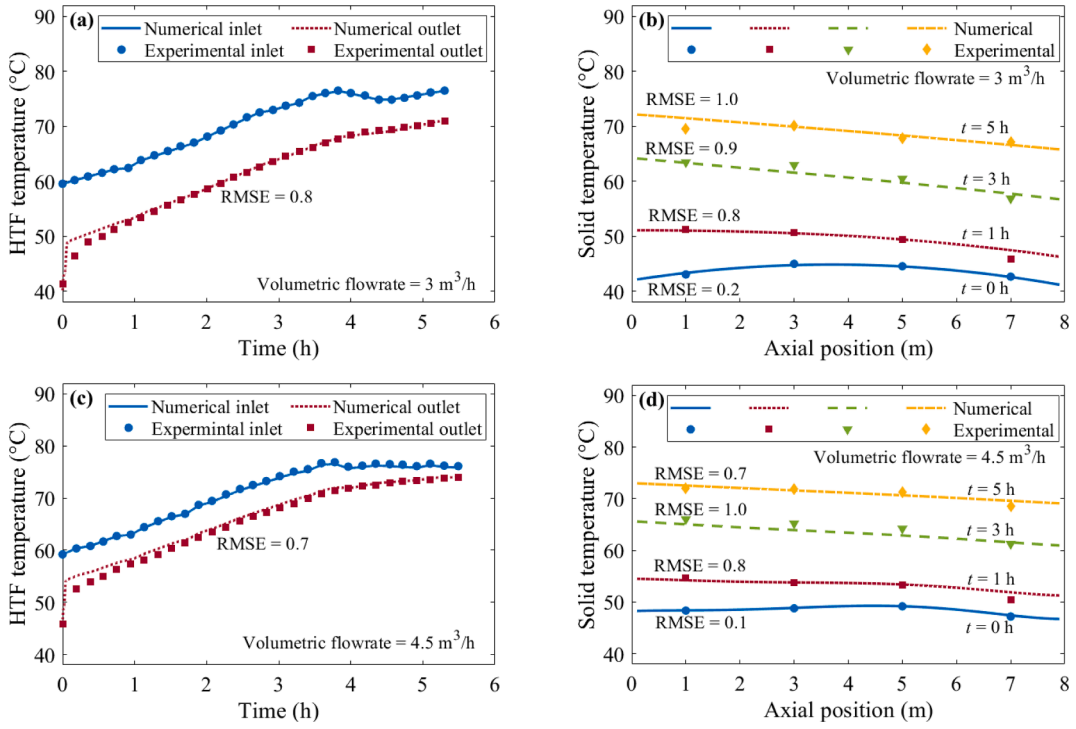

Fig. B1. Comparison of results obtained from the formulated concrete model and the experimental data published in Ref. [49]. Showing HTF and solid temperatures, respectively, for: (a, b), a HTF volumetric rate of 3 m^3/h, and (c, d) a HTF volumetric rate of 4.5 m^3/h. The HTF temperatures are measured at the inlet and the outlet of the storage unit and the solid temperatures are measured at different axial positions and different charging times.

model predictions are plotted using lines. The differences between the two sets of results are compared using the RMSE. The RMSEs of all compared data are 1 or less and the behaviour of the model predicted HTF and solid temperatures are almost the same as the experimental temperatures. The small difference is acceptable and could be a result of using slightly different thermophysical properties as well as the accuracy of the heat transfer coefficients.

Table C1
Calculated steam thermodynamic properties and other conditions at full rated electrical power of 50 MW and without TES charging/discharging. The stream numbers are the same as indicated in Figs. 1 and 2.

Stream number	Mass flowrate (kg/s)	Pressure (MPa)	Temperature (°C)	Quality (-)
1	61.2	12.0	530	superheated
2	1.8	11.5	520	superheated
3	59.5	11.5	520	superheated
4	9.6	2.86	331	superheated
4′	9.6	2.79	229	0
5	2.7	1.27	238	superheated
6	6.0	0.27	130	0.96
6′	6.0	0.20	120	0
7	41.2	0.18	58	0.88
8	48.9	0.18	58	0.79
9	48.9	0.18	58	0
10	48.9	1.34	58	subcooled
11	48.9	1.34	58	subcooled
12	48.9	1.27	117	subcooled
13	61.2	0.70	160	subcooled
14	61.2	15.5	163	subcooled
15	61.2	15.4	232	subcooled
16	61.2	12.3	327	1
19	1.8	0.18	58	0.97

Appendix C. – Khi Solar One at nominal power output

All steam properties and conditions obtained from the Khi Solar One power cycle model at full rated power output are listed in Table C1.

References

[1] Markides CN. Low-concentration solar-power systems based on organic Rankine cycles for distributed-scale applications: Overview and further developments. Front Energy Res 2015;3:47.
[2] Ramos A, Chatzopoulou MA, Freeman J, Markides CN. Optimisation of a high-efficiency solar-driven organic Rankine cycle for applications in the built environment. Appl Energy 2018;228:755–65.
[3] Wang Y, Song J, Chatzopoulou MA, Sunny N, Simpson MC, Wang J, Markides CN. A holistic thermoeconomic assessment of small-scale, distributed solar organic Rankine cycle (ORC) systems: Comprehensive comparison of configurations, component and working fluid selection. Energy Convers Manage 2021;248:114618.
[4] Freeman J, Hellgardt K, Markides CN. An assessment of solar-powered organic Rankine cycle systems for combined heating and power in UK domestic applications. Appl Energy 2015;138:605–20.
[5] Freeman J, Hellgardt K, Markides CN. Working fluid selection and electrical performance optimisation of a domestic solar-ORC combined heat and power system for year-round operation in the UK. Appl Energy 2017;186:291–303.
[6] International Renewable Energy Agency (IRENA). The Power to Change: Solar and Wind Cost Reduction Potential to 2025. 2016.
[7] Song J, Wang Y, Wang K, Wang J, Markides CN. Combined supercritical CO_2 (SCO_2) cycle and organic Rankine cycle (ORC) system for hybrid solar and geothermal power generation: Thermoeconomic assessment of various configurations. Renew Energy 2021;174:1020–35.
[8] Hirsch T, Feldhoff JF, Hennecke K, Pitz-Paal R. Advancements in the field of direct steam generation in linear solar concentrators-a review. Heat Transf Eng 2014;35:258–71.
[9] Dirker J, Juggurnath D, Kaya A, Osowade EA, Simpson M, Lecompte S, et al. Thermal energy processes in direct steam generation solar systems: Boiling, condensation and energy storage. Front Energy Res 2019;6:147.
[10] Birnbaum J, Eck M, Fichtner M, Hirsch T, Lehmann D, Zimmermann G. A direct steam generation solar power plant with integrated thermal storage. J Sol Energy Eng 2010;132:031014.
[11] Sun J, Liu Q, Hong H. Numerical study of parabolic-trough direct steam generation loop in recirculation mode: Characteristics, performance and general operation strategy. Energy Convers Manag 2015;96:287–302.
[12] Freeman J, Guarracino I, Kalogirou SA, Markides CN. A small-scale solar organic Rankine cycle combined heat and power system with integrated thermal energy storage. Appl Therm Eng 2017;127:1543–54.
[13] Achkari O, El Fadar A. Latest developments on TES and CSP technologies–Energy and environmental issues, applications and research trends. Appl Therm Eng 2020;167:114806.
[14] Pantaleo AM, Camporeale SM, Sorrentino A, Miliozzi A, Shah N, Markides CN. Hybrid solar-biomass combined Brayton/organic Rankine-cycle plants integrated with thermal storage: Techno-economic feasibility in selected Mediterranean areas. Renew Energy 2020;147(3):2913–31.
[15] Sarbu I, Sebarchievici C. A comprehensive review of thermal energy storage. Sustainability 2018;10:191.
[16] Steinmann WD, Eck M. Buffer storage for direct steam generation. Sol Energy 2006;80:1277–82.
[17] González-Roubaud E, Pérez-Osorio D, Prieto C. Review of commercial thermal energy storage in concentrated solar power plants: Steam vs. molten salts. Renew Sustain Energy Rev 2017;80:133–48.
[18] Laing D, Bahl C, Fiß M, Hempel M, Bauer T, Meyer-Grünefeldt M, et al. Combined storage system developments for direct steam generation in solar thermal power plants. ISES Solar World Congr 2011, Kassel, Germany.
[19] Karakurt AS, Güneş Ü. Performance analysis of a steam turbine power plant at part load conditions. J Therm Eng 2017;3:1121–8.
[20] Prieto C, Rodríguez A, Patiño D, Cabeza LF. Thermal energy storage evaluation in direct steam generation solar plants. Sol Energy 2018;159:501–9.
[21] Bai F, Xu C. Performance analysis of a two-stage thermal energy storage system using concrete and steam accumulator. Appl Therm Eng 2011;31:2764–71.
[22] Morisson V, Rady M, Palomo E, Arquis E. Thermal energy storage systems for electricity production using solar energy direct steam generation technology. Chem Eng Process 2008;47:499–507.
[23] Seitz M, Cetin P, Eck M. Thermal storage concept for solar thermal power plants with direct steam generation. Energy Procedia 2013;49:993–1002.
[24] Valenzuela L. Thermal energy storage concepts for direct steam generation (DSG) solar plants. Adv Conc Sol Therm Res Technol 2016:269–89.
[25] Bachelier C, Selig M, Mertins M, Stieglitz R, Zipf V, Neuhäuser A, et al. Systematic analysis of Fresnel CSP plants with energy storage. Energy Procedia 2015;69:1201–10.
[26] Guédez R, Arnaudo M, Topel M, Zanino R, Hassar Z, Laumert B. Techno-economic performance evaluation of direct steam generation solar tower plants with thermal energy storage systems based on high-temperature concrete and encapsulated phase change materials. AIP Conf Proc 2016;1734:070011.
[27] Li J, Gao G, Kutlu C, Liu K, Pei G, Su Y, et al. A novel approach to thermal storage of direct steam generation solar power systems through two-step heat discharge. Appl Energy 2019;236:81–100.
[28] Tian Y, Zhao CY. A review of solar collectors and thermal energy storage in solar thermal applications. Appl Energy 2013;104:538–53.

[29] Salomoni VA, Majorana CE, Giannuzzi GM, Miliozzi A, Di Maggio R, Girardi F, et al. Thermal storage of sensible heat using concrete modules in solar power plants. Sol Energy 2014;103:303–15.
[30] Laing D, Bahl C, Bauer T, Fiss M, Breidenbach N, Hempel M. High-temperature solid-media thermal energy storage for solar thermal power plants. Proc IEEE 2012;100:516–24.
[31] Laing D, Bauer T, Lehmann D, Bahl C. Development of a thermal energy storage system for parabolic trough power plants with direct steam generation. J Sol Energy Eng 2010;132:551–9.
[32] Eck M, Eickhoff M, Fontela P, Laing D, Meyer-Grünefeldt M, Möllenhoff M, et al. Test and demonstration of the direct steam generation (DSG) at 500 °C. SolarPaces Conf 2009, Berlin, Germany.
[33] EnergyNest. Thermal battery technology, https://energy-nest.com/technology/ [accessed 10.9.2021].
[34] Al Kindi AA, Pantaleo AM, Wang K, Markides CN. Thermodynamic assessment of steam-accumulation thermal energy storage in concentrating solar power plants. 11th Int Conf Appl Energy Proc 2019, Västerås, Sweden.
[35] MATLAB. Version 9.10.0 (R2021a), MathWorks Inc. 2021, Natick, Massachusetts.
[36] Lemmon EW, Bell IH, Huber ML, McLinden MO. NIST Standard Reference Database 23: Reference Fluid Thermodynamic and Transport Properties-REFPROP. National Institute of Standards and Technology (NIST) 2018, Version 10.0.
[37] Romanos P, Al Kindi AA, Pantaleo AM, Markides CN. Flexible nuclear plants with thermal energy storage and secondary power cycles: Virtual power plant integration in a UK energy system case study. e-Prime - Adv Electr Eng, Electron. Energy 2022;2:100027.
[38] Pump cavitation and how to avoid it: best practices in pump system design. Xylem Applied Water Systems, Xylem Inc. 2015.
[39] Al Kindi AA, Aunedi M, Pantaleo AM, Strbac G, Markides CN. Thermo-economic assessment of flexible nuclear power plants in future low-carbon electricity systems: Role of thermal energy storage. Energy Convers Manag 2022;258:115484.
[40] Golwalker KR, Kumar R. Practical guidelines for the chemical industry: operation, processes, and sustainability in modern facilities. First edition. Springer; 2022.
[41] Çengel YA, Boles MA, Kanoğlu M. Thermodynamics: an engineering approach. McGraw-Hill Education: Ninth edition; 2019.
[42] Van Putten H, Colonna P. Dynamic modeling of steam power cycles: Part II - Simulation of a small simple Rankine cycle system. Appl Therm Eng 2007;27:2566–82.
[43] Ray A. Dynamic modelling of power plant turbines for controller design. Appl Math Model 1980;4:109–12.
[44] Stevanovic VD, Petrovic MM, Milivojevic S, Maslovaric B. Prediction and control of steam accumulation. Heat Transf Eng 2015;36:498–510.
[45] Shampine FL, Reichelt MW. The MATLAB ODE suite. SIAM J Sci Comput 1997;18:1–22.
[46] González-Gómez PA, Laporte-Azcué M, Fernández-Torrijos M, Santana D. Hybrid storage solution steam-accumulator combined to concrete-block to save energy during startups of combined cycles. Energy Convers Manag 2022;253:115168.
[47] Jian Y, Falcoz Q, Neveu P, Bai F, Wang Y, Wang Z. Design and optimization of solid thermal energy storage modules for solar thermal power plant applications. Appl Energy 2015;139:30–42.
[48] Xu B, Li PW, Chan CL. Extending the validity of lumped capacitance method for large Biot number in thermal storage application. Sol Energy 2012;86:1709–24.
[49] Jian Y, Bai F, Falcoz Q, Xu C, Wang Y, Wang Z. Thermal analysis and design of solid energy storage systems using a modified lumped capacitance method. Appl Therm Eng 2015;75:213–23.
[50] Carbon Steel Handbook. Electric Power Research Institute (EPRI). 2007.
[51] The Engineering Toolbox. Thermal conductivities of common metals, metallic elements and alloys, https://www.engineeringtoolbox.com/thermal-conductivity-metals-d_858.html [accessed 10.8.2022].
[52] Hoivik N, Greiner C, Barragan J, Iniesta AC, Skeie G, Bergan P, et al. Long-term performance results of concrete-based modular thermal energy storage system. J Energy Storage 2019;24:100735.
[53] Gnielinski V. New equations for heat and mass transfer in the turbulent flow in pipes and channels. Int Chem Eng 1976;16:359–68.
[54] Farshad FF, Rieke HH. Surface-roughness design values for modern pipes. SPE Drill & Compl 2006;24:212–5.
[55] Shah MM. An improved and extended general correlation for heat transfer during condensation in plain tubes. HVAC&R Res 2009;15:889–913.
[56] Shah MM. General correlation for heat transfer during condensation in plain tubes: Further development and verification. ASHRAE Trans 2013;119:3–11.
[57] Seider WD, Lewin DR, Seader JD, Widagdo S, Gani R, Ng KM. Product and Process Design Principles: Synthesis, Analysis and Evaluation. Forth edition, Wiley, 2017.
[58] Chemical engineering essentials for the chemical professional. Chemical engineering plant cost index 2021, https://www.chemengonline.com/pci [accessed 16.4.2022].
[59] Turton R, Bailie RC, Whiting WB, Shaeiwitz JA, Bhattacharyya D. Analysis, Synthesis, and Design of Chemical Processes. Pearson Education: Forth edition; 2012.
[60] Couper JR, Penney WR, Fair JR, Walas SM. Chemical Process Equipment. Selection and Design. Third edition: Elsevier; 2012.
[61] Ulrich GD, Vasudevan PL. Chemical Engineering Process Design and Economics: A Practical Guide. Second edition. Process Publishing; 2004.
[62] John E, Hale M, Selvam P. Concrete as a thermal energy storage medium for thermocline solar energy storage systems. Sol Energy 2013;96:194–204.
[63] Libby C. Solar Thermocline Storage Systems: Preliminary Design Study. Electric Power Research Institute (EPRI) 2010.
[64] Nithyanandam K, Pitchumani R. Cost and performance analysis of concentrating solar power systems with integrated latent thermal energy storage. Energy 2014;64:793–810.
[65] Zhao B, Cheng M, Liu C, Dai Z. Thermal performance and cost analysis of a multi-layered solid-PCM thermocline thermal energy storage for CSP tower plants. Appl Energy 2016;178:784–99.
[66] European Investment Bank. Khi Solar One Tower Project (2012), https://www.eib.org/en/projects/pipelines/all/20100589# [accessed 18.4.2021].
[67] International Finance Corporation. Abengoa CSP SA. 2012, https://disclosures.ifc.org/project-detail/SPI/31083/abengoa-csp-sa [accessed 18.4.2021].
[68] International Renewable Energy Agency (IRENA). Renewable Power Generation Costs in 2019. 2020.
[69] Department of Energy of the Republic of South Africa. Independent Power Producers Procurement Programme (IPPPP): An Overview. 2018.
[70] Meteonorm. Worldwide irradiation data (2019), https://meteonorm.com/en/ [accessed 18.6.2020].
[71] Carlson F, Davidson JH. On the use of thermal energy storage for flexible baseload power plants: Thermodynamic analysis of options for a nuclear Rankine cycle. J Heat Transf 2020;142:052904.
[72] Zhao Y, Liu M, Wang C, Li X, Chong D, Yan J. Increasing operational flexibility of supercritical coal-fired power plants by regulating thermal system configuration during transient processes. Appl Energy 2018;228:2375–86.
[73] Biglia A, Comba L, Fabrizio E, Gay P, Aimonino DR. Steam batch thermal processes in unsteady state conditions: Modelling and application to a case study in the food industry. Appl Therm Eng 2017;118:638–51.